AFIT/GA/ENY/91D-10

1

PROPULSIVE CAPABILITY OF A REEL-IN TETHER WITH SAFE SEPARATION BETWEEN PAYLOAD AND ORBITER

THESIS

Jay H. Rothhaupt, Captain, USAF

AFIT/GA/ENY/91D-10

Approved for public release; distribution unlimited

①

AFIT/GA/ENY/91D-10

PROPULSIVE CAPABILITY OF A REEL-IN TETHER WITH SAFE SEPARATION BETWEEN PAYLOAD AND ORBITER

THESIS

Presented to the Faculty of the School of Engineering
of the Air Force Institute of Technology
Air University
In Partial Fulfillment of the
Requirements for the Degree of
Master of Science in Astronautical Engineering

Jay H. Rothhaupt, B.S.
Captain, USAF

December 1991

Approved for public release; distribution unlimited

Preface

This study of safe payload and orbiter separation for a reel-in tether is an extension of work performed in 1987 by Dr William E. Wiesel. The techniques used parallel those of Dr Wiesel, and the dynamics model development, integral evaluation, optimization, and numerical techniques are presented in detail.

This document was prepared with WordPerfect software, while Harvard Graphics and MATLAB were used for the figures. A modified version of Dr Wiesel's FORTRAN algorithm was used for numerical analysis. In addition to saving countless hours at the computer, the code served as an optimization text and saved many hours of advising time. Above all, the numerical techniques within the code provided a more concise optimization method than I would have mechanized on my own. I applaud Dr Wiesel for his recommendation to use his code and thank him wholeheartedly for providing it.

In addition to the code, Dr Wiesel's advice, instruction, and support are greatly appreciated. His expert presentations were inspiring throughout the course of study and the completion of this document. I also thank Captains Tim Middendorf and Ralph Fero for their WordPerfect and MATLAB advice.

Jay H. Rothhaupt

Table of Contents

List of Figures

Figure Page

List of Tables

Table Page

Abstract

This study investigates the use of a massless reel-in tether for propulsion of a payload following deployment from an orbiter. The distance between the payload and orbiter at closest passage is addressed. A literature review revealed several tether concepts, extensive tether research, and numerous mathematical models. However, previous work in the area of reel-in tethers is limited to propulsion feasibility. The reel-in tether is operated following optimum ejection of the payload from the orbiter using a free arc and subsequent full arc. The free arc of zero tether tension provides initial separation. Switching to a full arc of continuously-maximum tension at the optimum time accelerates and propels the payload until the mission is complete. Tether and winch capabilities are assumed to be satisfactory during the arcs. Families of trajectories are examined for a range of mission times and minimum final payload energy. Families for two ejection speeds provide comparison of propulsion capability, tether length, and minimum separation radius. Safe separation is achievable through variation of the mission duration and/or the ejection speed.

PROPULSIVE CAPABILITY OF A REEL-IN TETHER WITH SAFE SEPARATION BETWEEN PAYLOAD AND ORBITER

I Introduction

Chemical rockets are the primary method for effecting payload transfers between various earth orbits. However, the mass of the propellant for these rockets contributes to high launch costs and complexity. The space program needs alternative payload transfer options to reduce mass and launch costs.

Tethers provide a conceptually lightweight alternative to chemical rockets for payload transfer. Normally, a tether is a device connecting a payload to an orbiting platform and transferring orbital energy to the payload. Optimally, a tether would be reusable, durable, and less massive than a chemical rocket.

1 Background

There are various ways of transferring orbital energy using a tether. One unique concept involves use of electrical current through the tether to interact with the earth's magnetic field and generate propulsive force (3:34). Most concepts, however, involve controlling the swinging motion of a payload at the end of a tether (4:41). Payload release from the tether completes the energy transfer.

Payload swinging motion induces tension within the tether. Mathematical models predict this varying, controllable, and generally desirable tension. Since the tether must be originally constructed to withstand a maximum tension, the maximum tension capability can be used to enhance the transfer.

Reel-in of the tether with an electric motor enhances the transfer since greater payload orbital energy changes are obtainable relative to a swing release. Reel-in at the maximum tension capability of the tether optimizes the obtainable energy change. However, the reel-in accelerates the payload to higher speed, which subsequently causes greater payload travel for a specific time period. Large time periods can require the tether to be lengthy and massive, which reduce the tether's mass advantage over a chemical rocket (14).

2 Problem Statement

Although use of a short tether reduces mass, it brings the payload within close proximity of the orbiter during reel-in. This increases the undesirable likelihood of payload and/or tether impact with the orbiter.

3 Research Objective and Questions

In order for the reel-in tether to be useful, the impact possibility must be eliminated while retaining sufficient payload energy transfer. Answers to the following questions must be determined:

1) What is the energy transfer capability of a reel-in tether when a specified separation distance and zero tether reel-in speed exist at release?

2) Is the resultant energy transfer capability sufficient for propulsion?

4 Assumptions

The following assumptions will be employed:

1) The tether is a massless, inextensible device that provides only tension. This assumption eliminates the complexity of tether dynamics. Although extensively reducing the complete tether model, this assumption satisfactorily allows dynamics modelling.

2) The system is orbiting the earth in a circular orbit. This is operationally typical for the transfer of energy to a payload and simplifies the dynamics.

3) The payload and orbiter motions are limited to the plane of the original orbit.

4) The tension motor is capable of maintaining full tension at all tether speeds and provides no load during periods requiring zero tension.

5) The resultant payload orbit shape is of minimal concern.

Solution of the reel-in tether dynamics begins with the development of equations of motion for the system. However, several other tether concepts pre-date the reel-in method.

II Literature Review

1 Dynamic Tether Applications

In 1895, Tsiolkovsky suggested using a tether-like device to connect two orbiting masses and subsequently use the gravity-gradient forces for stabilization. Through 1972, however, tether study was minimal and the only use of tethers was during the Gemini program for limited experiments. The Space Shuttle program provided the advent of modern tether study (3:33).

Grossi, in describing the historical background of the Tethered Satellite System (TSS), states that a Space Shuttle-borne tether was first proposed in October 1972. Originally it was considered a novelty, primarily for use as a space-borne radar at an ultra-low frequency (ULF), that would detect submerged submarines. Increased interest paved the way to an organized project called SKYHOOK at the Smithsonian Astrophysical Observatory (SAO) in Cambridge, MA. SKYHOOK was the predecessor to numerous electrodynamic studies that evolved into the TSS project. The TSS operation was originally planned as a local vertical deployment of a metal, 20 km device (10:2).

As the TSS evolved, it was applied to an atmospheric probe mission. The TSS would lower a satellite from the Space Shuttle to an altitude of 115 km for atmospheric measurement. Overall, this is called the TSS/Wing System or the Tethered Satellite/Wing System (TS/WS) since the satellite contains an aerodynamic surface for control (13:1). This launch was scheduled for 1991 (4:41) and subsequently delayed to 1992 (11:27).

R. L. Forward describes the planetary use of tethers. One concept uses a long, tether-like device called a catapult. The catapult would extend from a planet surface into space, allowing a payload to be accelerated along the catapult length to achieve the desired velocity. Limitations are primarily based on the cable material, which restricts length and acceleration capability. Forward also describes a rotovator, consisting of a tether with an adjustable rotation and extending from a planet or moon surface. A planet rotovator could be used "to lift payloads from a planet or to deposit payloads onto a planet". Sometimes referred to as a skyhook, the rotovator would allow smooth touchdowns and take-offs of the payload from it's tip. This is accomplished with the adjustable rotation, which apparently is the bending of the rotovator tip to or from the planet surface (8:1).

Bekey describes use of an electrodynamic tether for propulsion. High orbital speeds would allow a vertical tether to generate electrical current as it moves through a planet's magnetic field. However, it would be an open-loop generator, collecting free electrons (trapped within the magnetic field) and ejecting them at the other end with an electron gun. Of course, the current would power devices within the platform deploying the tether. However, the disadvantage of the current generation is the resultant force that lowers the system orbit. Alternately, available electrical power (solar generated, for example) could be used to induce an orbit-raising force (3:34).

2 Dynamic Tether Description

Bekey provides a basis for developing a description of the fundamental dynamics of a fixed-length massless tether (3:35). The simplest description begins with a vertical tether and extends to a tether with an angular offset from vertical.

The system center of mass (CM), between two tether-connected masses, behaves as an orbiting body. However, the end masses are forced by any tether tension that exists. This is easily understood based on the fact that the two masses and the CM all orbit with the same period due to the tether connection.

For a vertical tether, the mass at the higher altitude is being forced to move at a higher speed than the speed of a free orbit for that altitude. Likewise, the mass at the lower altitude is being forced to move at a lower speed than that of a free orbit. Essentially, the vertical tension respectively aids or opposes gravity in the two cases. Thus, the "above" mass "feels" more gravity and acts as if it were closer to the earth, while the "below" mass acts as if it were farther from the earth. In fact, each mass orbits as if it is positioned at the CM, i.e., with the same period as the CM. This means that the system undergoes one rotation about the CM during each orbit. Thus, the tether force provides artificial gravity to each mass, approximately 4 x 10^{-4} g per km of tether length in low orbit (3:36).

For a tether with an angular offset from vertical, the tether connection must still maintain the two masses orbiting with the same period as the CM. Thus, the same vertical forces must exist (provided the two masses are at the same altitudes as before). However, since the tether is at an angle from vertical, a greater tension must exist to provide the vertical force. Additionally, the angle from vertical induces a horizontal force for both masses which causes the system to rotate toward and oscillate about the vertical. The oscillation, as in a pendulum, is dependant on tether length. Bekey also describes the varying of this oscillatory motion by adjusting the tether length, either for stability damping or for inducing high speeds (3:35).

Although the overall system momentum and energy is constant during fixed length oscillation, each mass's momentum and energy vary. Obviously, the relative momentum and change of momentum for each mass is equal and opposite that of the other mass. Introduction of work to the system by varying the length during tension can increase oscillations. This provides the basis for a swing release or bolo method of propelling a payload from an orbiter.

Whether released from above on a vertical tether (no swing), from directly aft to directly forward (180° swing), or from a complete 360° swing; a payload will gain orbital energy. If the initial orbit is circular, the resultant elliptical orbit will have an apoapsis to periapsis difference of 7, 14, or greater than 25 times the length of the tether, for the respective swings (3:38). If reel-in of the tether is performed rather than use of a fixed tether length, greater apoapsis increases are possible (14:355)

Colombo's extensive tether works indicate methods of implementing the swing release. These range from ideas of storing the tether in the Space Shuttle or in space to large scale tethers (430-5900 km) for LEO-GEO orbit. Included are mass estimates for a Space Shuttle palette to house a tether (6000 Kg) and cost savings estimates (over a propellant-driven device). Additionally, a mechanism for ferrying (moving) a payload from the Space Shuttle to a tethered platform is described (6:1-47).

In 1986, Bekey and Penzo reported that a tether deployment was being studied for the 20,000 lb Advance X-Ray Astrophysics Facility satellite. The satellite's 320 n. mi. orbit would require a 32 n. mi. tether and sustain 500 lb tension while saving 5,000 lb of propellant. Furthermore, a Getaway Special container with a tether was planned after resumption of Space Shuttle flights. The container was to test the operation of a tension device, a tether length meter, and the line cutter that severs the tether. The container design was based on a 10 km tether for a 350 lb payload. Finally, Bekey and Penzo also describe a combination skyhook/catapult function for the Martian moons Phobos and Deimos. In this approach, the tether is anchored to the surface of a moon and the payload crawls to the tether tip. The payload and moon are then the two masses for the system and a release similar to a vertical release accomplishes the energy transfer (4).

3 Modeling Background

Kopke and Wiesel present equations of motion (EOM) derivations for general tether mechanics in Newtonian (12:879) and Lagrangian forms, respectively. In addition to the EOM presentation, Wiesel analyzes the EOMs for optimum control based on the tether tension. Wiesel identifies three tether operations as optimum. The first case, a coasting trajectory or free arc, occurs when the tension is zero. The full, or maximum tension arc occurs when the tension is constant and at the safe operating tension limit of the tether. Finally, a singular arc occurs during a period of time when the tension is maintained such that the Switching Function for the Control Hamiltonian is zero. To maintain this condition, the tension is required to vary in a prescribed manner for any set of initial payload conditions (14:352).

Typically, the EOMs are solved assuming a circular orbit of the system (elliptical orbit dynamics are presented by De Matteis (7)). The solution is normally performed computationally, since a closed form solution is excluded by the tension. For the optimum cases of constant tension, the solution reduces to elliptic integrals that can be determined numerically. This approach is applied to determine whether safe separation between payload and orbiter can feasibly be accomplished.

III Methodology

Deployment of a payload from an orbiter begins with the payload and orbiter located at the same point, the system center of mass (CM). A spring or other mechanism then applies a deployment force to eject the payload from the orbiter, causing both to drift from the CM, which remains in the original orbit. A free arc of zero tension allows the payload to drift away from the orbiter with the tether trailing behind. This allows a subsequent full arc with a high constant tension to accelerate and propel the payload.

Although a local level coordinate system with horizontal and vertical axes at the CM can be used to identify the positions of the payload and orbiter, both positions need not be specified since they are coupled (dependent). The coupling is due to the deployment force, which acts equally and oppositely on each mass. This is also the case with a tethering force. Either force causes the lower mass item (the payload in most cases) to undergo more extensive motion than the higher mass item. Since the motion of interest is that of the payload relative to the orbiter, a coordinate frame at the orbiter is used.

Examination of the payload's separation from the orbiter requires the development of the equations of motion (EOMs) in terms of the orbiter frame, solution of the EOMs, and determination of the payload trajectory relative to the orbiter. The trajectories of interest are those with optimum (maximum or minimum) payload orbital energy, although payload and orbiter separation can be investigated for any resultant payload orbital energy.

1 Coordinate Systems

The position vector of the CM, in any coordinate system, is defined by the mass-weighted average position of the masses as shown in Eq (1).

$$\vec{r}_{CM} \equiv \sum (m_n \ \vec{r}_n) \Big/ \sum (m_n) \qquad \textbf{(1)}$$

If the coordinate origin is located at the CM (a coordinate system called the CM or "c" frame), then by definition the vector is zero. Thus, for a payload and orbiter system (masses m_1 and m_2, respectively), the relationship between their position vectors is given by Eq (2) when coordinatized in the CM frame.

$$\begin{aligned} {}^c\vec{r}_1 m_1/(m_1+m_2) &= -{}^c\vec{r}_2 m_2/(m_1+m_2) \\ {}^c x_1 m_1 &= -{}^c x_2 m_2 \\ {}^c y_1 m_1 &= -{}^c y_2 m_2 \\ {}^c r_1 m_1 &= {}^c r_2 m_2 \end{aligned} \qquad \textbf{(2)}$$

Eq (2), also provides scalar relationships between payload and orbiter quantities. Since the position of the payload relative to the orbiter is desired, a coordinate system with origin at the orbiter (the "o" frame) is chosen. The relationship between the "c" and "o" frame is provided in Eq (3).

$$ {}^{o}\vec{r}_1 \equiv {}^{c}\vec{r}_{2\rightarrow 1} \equiv {}^{c}\vec{r}_1 - {}^{c}\vec{r}_2 \qquad (3) $$

The orbiter position in vector Eq (3) can be eliminated using Eq (2). Eq (4) provides the resultant scalar equations. Eq (5) is the version with the payload position eliminated.

$$ {}^{o}x_1 = {}^{c}x_1\frac{m_1 + m_2}{m_2} \qquad {}^{o}y_1 = {}^{c}y_1\frac{m_1 + m_2}{m_2} \qquad {}^{o}r_1 = {}^{c}r_1\frac{m_1 + m_2}{m_2} \qquad (4) $$

$$ {}^{o}x_1 = -{}^{c}x_2\frac{m_1 + m_2}{m_1} \qquad {}^{o}y_1 = -{}^{c}y_2\frac{m_1 + m_2}{m_1} \qquad {}^{o}r_1 = {}^{c}r_2\frac{m_1 + m_2}{m_1} \qquad (5) $$

As described before, the rectangular coordinate axes for the "c" and "o" frames are respectively parallel to each other, but have not been specifically oriented. Since both frames are in orbit about a planet, a planet coordinate system (the "p" frame) can be defined with the one axis aligned to the origin of the "c" frame. For simplicity, this vertical axis direction up ($\hat{e}_\rho$) and the horizontal axis direction forward in the direction of the orbit ($\hat{e}_\eta$) provide the orientation of all three frames. This orientation is shown in Figure 3.1.

The position and velocity vectors of either mass are shown in Eqs (6) and (7). The angular rotation of the "p", "c", and "o" frames with respect to an inertial (non-rotating) coordinate system (the "i" frame) is also shown in Eq (8).

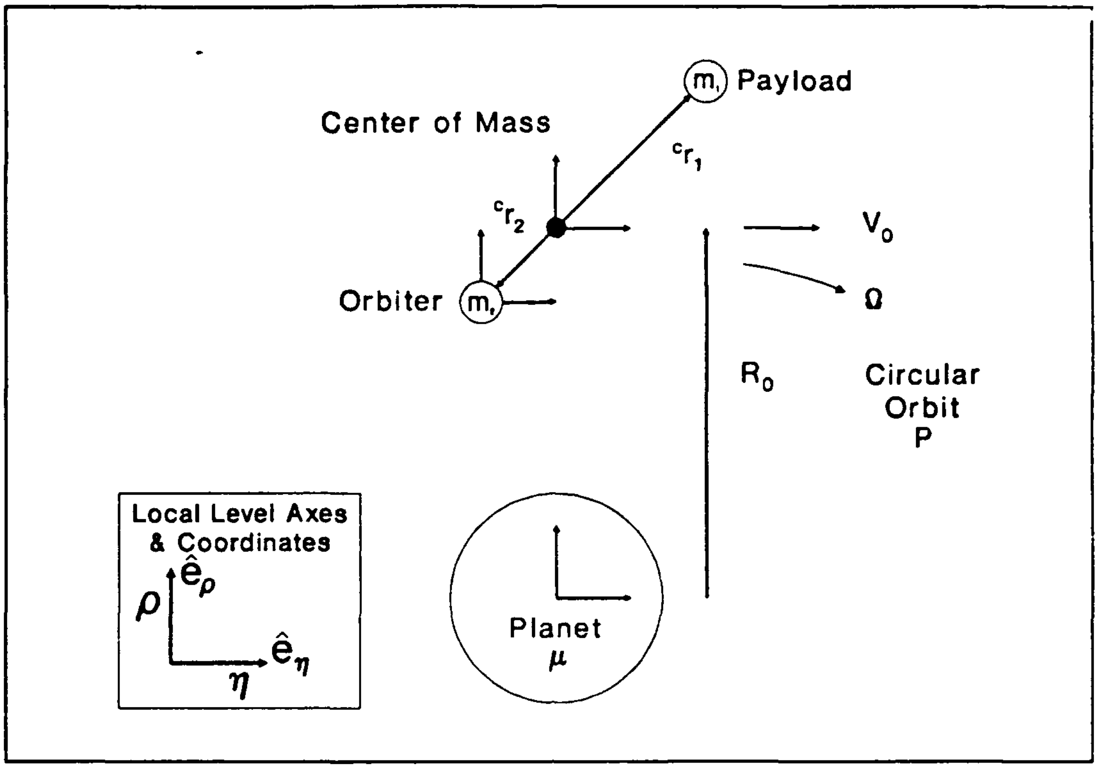

Figure 3.1 - Coordinate Frames

$$^p\vec{r}_n = {}^c\vec{r}_n + R_o\hat{e}_\rho = (R_o + {}^c\rho_n)\hat{e}_\rho + {}^c\eta_n\hat{e}_\eta \tag{6}$$

$$\begin{aligned} ^p\vec{v}_n \equiv {}^p\dot{\vec{r}}_n &= ({}^c\dot{\rho}_n\hat{e}_\rho + {}^c\dot{\eta}_n\hat{e}_\eta + \Omega(R_o + {}^c\rho_n)\hat{e}_\eta - \Omega{}^c\eta_n\hat{e}_\rho \\ &= ({}^c\dot{\rho}_n - \Omega{}^c\eta_n)\hat{e}_\rho + ({}^c\dot{\eta}_n + \Omega(R_o + {}^c\rho_n))\hat{e}_\eta \end{aligned} \tag{7}$$

$$^p\vec{\omega}_{ip} = {}^c\vec{\omega}_{ic} = \Omega(\hat{e}_\rho \times \hat{e}_\eta) \equiv \Omega\hat{e}_\omega \tag{8}$$

2 Kinetic and Potential Energy

Substitution of Eqs (4) and (5) into Eq (7), with the local horizontal and vertical coordinates (η and ρ) used instead of the general rectangular coordinates (x and y, respectively), provides the velocity vector for each mass in Eqs (9) and

(10). Eq (11) shows the system kinetic energy. As desired, the equations are functions of the payload position with respect to the orbiter.

$$ {}^{P}\vec{v}_1 = \frac{m_2}{m_1 + m_2}\left[({}^{o}\dot{\rho}_1 - \Omega\,{}^{o}\eta_1)\hat{e}_r + ({}^{o}\dot{\eta}_1 + \Omega\,{}^{o}\rho_1)\hat{e}_\eta\right] + R_o\Omega\hat{e}_\eta \tag{9} $$

$$ {}^{P}\vec{v}_2 = \frac{m_1}{m_1 + m_2}\left[(-{}^{o}\dot{\rho}_1 + \Omega\,{}^{o}\eta_1)\hat{e}_r + (-{}^{o}\dot{\eta}_1 - \Omega\,{}^{o}\rho_1)\hat{e}_\eta\right] + R_o\Omega\hat{e}_\eta \tag{10} $$

$$ \begin{aligned} T = \frac{1}{2}\frac{m_1 m_2}{m_1 + m_2}\Big[& {}^{o}\dot{\rho}_1^2 + {}^{o}\dot{\eta}_1^2 + 2\Omega({}^{o}\rho\,{}^{o}\dot{\eta}_1 - {}^{o}\dot{\rho}_1{}^{o}\eta_1) \\ & + \Omega^2({}^{o}\rho_1^2 + {}^{o}\eta_1^2)\Big] + \frac{1}{2}(m_1 + m_2)R_o^2\Omega^2 \end{aligned} \tag{11} $$

Prior to substituting Eqs (4) and (5) in Eq (6) to obtain the desired potential energy expression, it's useful to expand the potential energy to third order as shown in Eq (12).

$$ \begin{aligned} V_n \equiv \frac{-\mu m_n}{|\vec{r}_n|} &= -\mu m_n[(R_o + {}^{c}\rho_n)^2 + {}^{c}\eta_n^2]^{-1/2} \\ &= \frac{-\mu m_n}{R_o}\left(1 + \frac{2\,{}^{c}\rho_n}{R_o} + \frac{{}^{c}\rho_n^2 + {}^{c}\eta_n^2}{R_o^2}\right)^{-1/2} \\ &\equiv \frac{-\mu m_n}{R_o}(1 + \varepsilon)^{-1/2} \\ &= \frac{-\mu m_n}{R_o}\left(1 - \frac{1}{2}\varepsilon + \frac{3}{8}\varepsilon^2 - \frac{15}{32}\varepsilon^3 + O(\varepsilon^4)\right) \end{aligned} \tag{12} $$

Eq (12) can be algebraically re-written in successive powers of the position variables as Eq (13).

However, for a circular orbit, μ can be eliminated based on Ω in Eq (14). The resultant potential energy for either mass is shown in Eq (15).

$$V_n = \frac{-\mu m_n}{R_o}\left(1 - \frac{{}^c\rho_n}{R_o} + \frac{2\,{}^c\rho_n^2 - {}^c\eta_n^2}{2R_o^2} - \frac{9\,{}^c\rho_n^3 - 6\,{}^c\rho_n\,{}^c\eta_n^2}{4R_o^3}\right) \tag{13}$$

$$\Omega \equiv \sqrt{\frac{\mu}{R_o^3}} \quad \therefore \quad \mu = \Omega^2 R_o^3 \tag{14}$$

$$V_n = \Omega^2 m_n\left(-R_o^2 + R_o\,{}^c\rho_n - \frac{2\,{}^c\rho_n^2 - {}^c\eta_n^2}{2} + \frac{9\,{}^c\rho_n^3 - 6\,{}^c\rho_n\,{}^c\eta_n^2}{4R_o}\right) \tag{15}$$

With the potential energy expanded to third order, the "o" frame payload coordinates of Eqs (4) and (5) can be substituted. Also, since position variables for each mass have opposite sign, odd powers of each mass's potential energy negate when summed. Eq (16) is the total potential energy.

$$V = \frac{1}{2}\frac{m_1 m_2}{m_1 + m_2}\Omega^2({}^o\eta_1^2 - 2\,{}^o\rho_1^2) - (m_1 + m_2)R_o^2\Omega^2 \tag{16}$$

Both the kinetic and potential energy have constant terms due to the circular orbit of the CM. These constant terms need not be included in the Lagrangian shown in Eq (17) since their derivatives in Lagrange's equation will be zero. Eq (17) also introduces the reduced mass, $M=m_1m_2/(m_1+m_2)$, which represents the mass ratio coefficient common to the kinetic and potential energies. Since the Lagrangian is a function of the desired payload coordinates in the "o" (orbiter) frame, the orbiter pre-superscript and the payload subscript are omitted in subsequent equations.

$$L = \frac{1}{2}M\left[{}^{\circ}\dot{\rho}_1^2 + {}^{\circ}\dot{\eta}_1^2 + 2\Omega({}^{\circ}\rho_1{}^{\circ}\dot{\eta}_1 - {}^{\circ}\dot{\rho}_1{}^{\circ}\eta_1) + \Omega^2({}^{\circ}\rho_1^2 + {}^{\circ}\eta_1^2)\right] - \frac{1}{2}M\Omega^2({}^{\circ}\eta_1^2 - 2\,{}^{\circ}\rho_1^2) \quad \textbf{(17)}$$

3 Equations of Motion

Eq (18), Lagrange's equation, can be used to obtain the equations of motion (EOMs). In this case, the general Lagrange equation coordinate q represents either the horizontal or vertical coordinate (η or ρ).

$$\frac{d}{dt}\left[\frac{\partial L}{\partial \dot{q}}\right] - \frac{\partial L}{\partial q} = Q_q \equiv \vec{F}\cdot\frac{\partial \boldsymbol{r}}{\partial q} \qquad \textbf{(18)}$$

For simplicity, the Lagrangian of Eq (17) can be changed to the perfect square form. This Lagrangian is shown in Eq (19).

$$L = \frac{1}{2}M[(\dot{\rho} - \Omega\eta)^2 + (\dot{\eta} + \Omega\rho)^2 - \Omega^2(\eta^2 - 2\rho^2)] \qquad \textbf{(19)}$$

Also, the tether tension, T, acts on the payload along the radial direction between the orbiter and payload, as shown in Eq (20).

$$\vec{F} = -T\hat{e}_r \qquad \boldsymbol{r} = r\hat{e}_r \equiv \sqrt{\rho^2 + \eta^2}\,\hat{e}_r \qquad \textbf{(20)}$$

For q=ρ, Lagrange's equation becomes the first EOM, Eq (21), while for q=η, Lagrange's equation becomes the second EOM, Eq (22). The tether acceleration, τ^*, is defined based on the constant tether tension and the reduced mass. Constant tension is an optimum condition for a tether and would be the maximum safe tension for the tether (14:352).

$$\ddot{\rho} - 2\Omega\dot{\eta} - 3\Omega^2\rho = -(\rho/r)(T/M) \equiv -(\rho/r)\tau^* \tag{21}$$

$$\ddot{\eta} + 2\Omega\dot{\rho} = -(\eta/r)(T/M) \equiv -(\eta/r)\tau^* \tag{22}$$

4 Free Arc Solution

When the tension is zero, the EOMs of Eqs (21) and (22) form a second-order, constant-coefficient, homogeneous system. The simple closed solution is known as the Chlohessy-Wiltshire equatíons (16:78). With no tension, the masses are essentially independently orbiting bodies (gravity between the masses is not modelled). The zero tension, or free arc solution shown in Eq (23) describes the relative motion of the two masses. If the motion of each mass relative to the CM is desired, conversion to the "c" frame is accomplished with Eqs (4) and (5). The angular location of the system in its orbit is defined as $\psi=\Omega(t-t_o)$.

$$\mathcal{X}(t) \equiv \begin{bmatrix} \rho(t) \\ \eta(t) \\ \dot{\rho}(t) \\ \dot{\eta}(t) \end{bmatrix} = \begin{bmatrix} 4-3\cos\psi & 0 & \frac{1}{\Omega}\sin\psi & \frac{2}{\Omega}(1-\cos\psi) \\ 6(\sin\psi-\psi) & 1 & \frac{2}{\Omega}(\cos\psi-1) & \frac{4}{\Omega}\sin\psi-\frac{3}{\Omega}\psi \\ 3\Omega\sin\psi & 0 & \cos\psi & 2\sin\psi \\ 6\Omega(\cos\psi-1) & 0 & -2\sin\psi & 4\cos\psi-3 \end{bmatrix} \begin{bmatrix} \rho(t_o) \\ \eta(t_o) \\ \dot{\rho}(t_o) \\ \dot{\eta}(t_o) \end{bmatrix} \tag{23}$$

5 Full Arc Solution

To remove the tension acceleration, τ^*, from one of the EOMs, Eqs (21) and (22) are converted from rectangular to polar coordinates using Eqs (24) and (25). The angular coordinate, θ, is measured from the horizontal axis aft of the orbit direction with positive rotation downward (14:354).

$$\rho \equiv -r\sin\theta \qquad \eta \equiv -r\cos\theta \tag{24}$$

$$\dot{\rho} = -\dot{r}\sin\theta - r\dot{\theta}\cos\theta \qquad \dot{\eta} = -\dot{r}\cos\theta + r\dot{\theta}\sin\theta \tag{25}$$

Direct substitution of the polar coordinates into the rectangular EOMs can be performed, or a new Lagrangian can be obtained as in Eq (26) and subsequently used in Lagrange's equation.

$$L = \frac{1}{2}M(\dot{r}^2 + r^2\dot{\theta}^2 + 2\Omega r^2\dot{\theta} + 3\Omega^2 r^2\sin^2\theta) \tag{26}$$

The polar EOMs are given in Eqs (27) and (28).

$$\ddot{r} - r\dot{\theta}^2 - 2\Omega r\dot{\theta} - 3\Omega^2 r\sin^2\theta = -(T/M) \equiv -\tau^* \tag{27}$$

$$r\ddot{\theta} + 2\dot{r}(\Omega + \dot{\theta}) - 3\Omega^2 r\sin\theta\cos\theta = 0 \tag{28}$$

5.1 Inertial Frame EOM Reduction. To simplify the EOMs of Eqs (27) and (28), a non-rotating frame, the "n" frame, with no potential energy variation throughout the frame is used. The kinetic energy and EOMs in polar coordinates of a single origin-tethered mass, M, within the frame are given in Eq (29).

$$\begin{aligned} T &= \frac{1}{2}M\left[{}^{n}\dot{r}^{2} + \left({}^{n}r\,{}^{n}\dot{\theta}\right)^{2}\right] \\ {}^{n}\ddot{r} - {}^{n}r\,{}^{n}\dot{\theta}^{2} &= -\tau^{*} \\ {}^{n}r\,{}^{n}\ddot{\theta} + 2\,{}^{n}\dot{r}\,{}^{n}\dot{\theta} &= 0 \end{aligned} \tag{29}$$

If the "n" frame were rotated with an additional angular rate Ω, the kinetic energy and EOMs would be as shown in Eq (30). This rotational sense is the case with the tether model due to the angular reference axis and the orbital angular motion. The sense is clear if a payload located at the angular reference axis is considered. The payload can move from the reference axis because of the payload's inertial angular motion. Conversely, the reference axis can move from the payload because of the rotational angular motion of the frame. Both motions induce positive changes in θ. Figure 3.2 diagrams the relationship between the frames.

$$\begin{aligned} T &= \frac{1}{2}M\left[\dot{r}^{2} + \left[r\left(\dot{\theta} + \Omega\right)\right]^{2}\right] \\ \ddot{r} - r\left(\dot{\theta} + \Omega\right)^{2} &= \ddot{r} - r\dot{\theta}^{2} - 2r\dot{\theta}\Omega - r\Omega^{2} = -\tau^{*} \\ r\ddot{\theta} + 2\dot{r}\left(\dot{\theta} + \Omega\right) &= 0 \end{aligned} \tag{30}$$

Comparison of Eqs (27) and (28) with Eqs (29) and (30) shows that the Ω^2 terms in Eqs (27) and (28) include centripetal (rotating frame) acceleration terms, as well as the gravity gradient (truncated potential energy) term(s) from

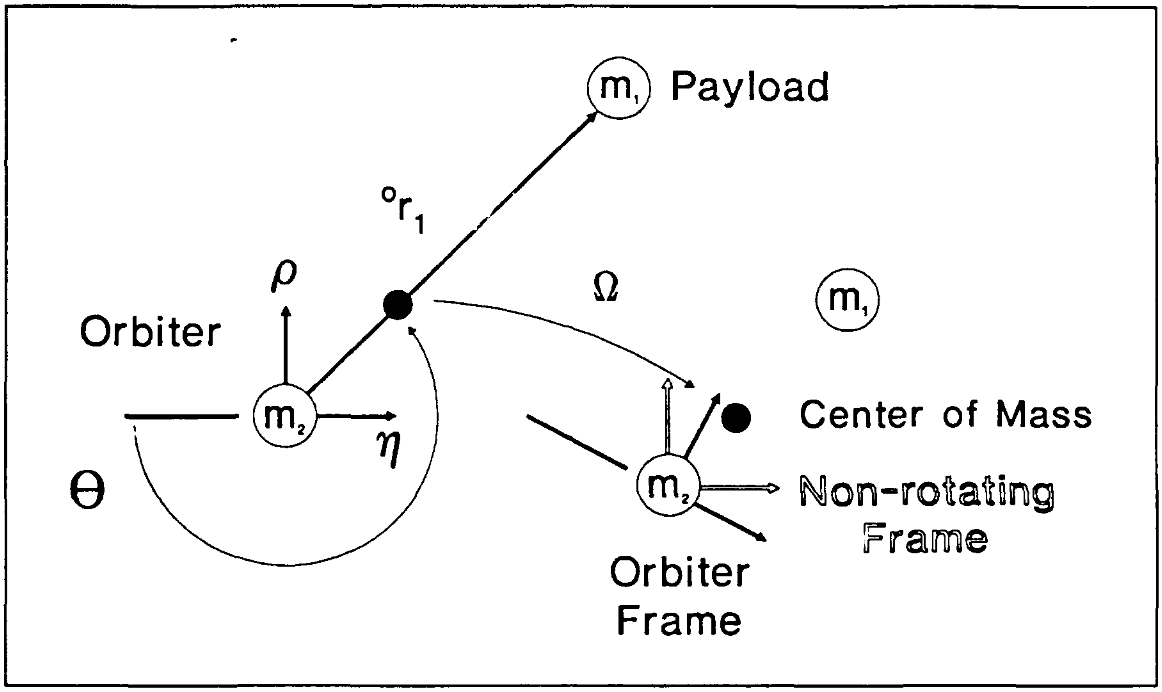

Figure 3.2 - Orbiter and Non-rotating Frame Relationship

Eq (16). These are considered negligible compared to the other terms due to the relatively low angular rate and high tether acceleration for a typical deployment (14:353). This is the case if the tether acceleration is significantly greater than the centripetal and gravity gradient affects. However, to eliminate the Ω terms, a non-rotating frame, the "n" frame is used. The initial "n" frame orientation is the same as the "o" frame orientation at the beginning of the full arc. With the "n" frame fixed at this orientation during the full arc, Eq (29) allows determination of the motion, provided the "n" frame coordinates are returned to "o" frame coordinates at the end of the full arc. The angle between the "n" frame and the desired "o" frame is simply $\Omega(t_f - t_i)$. Since this is the only difference between the two frames, the "n" pre-superscript is not retained in the following equations.

The usual angular momentum of the payload (relative to the orbiter) is given by Eq (31) and is clearly an integral of the second EOM of Eq (29) and therefore constant.

$$h = |\vec{h}| \equiv |r\hat{e}_r \times r\dot{\theta}\hat{e}_\theta| = |r^2\dot{\theta}\hat{e}_{\dot{\theta}}| = r^2\dot{\theta} \tag{31}$$

The usual kinetic energy of a system (as shown in Eq (29)) is not a constant of the first EOM of Eq (29) because of the tension acceleration. However, since the acceleration is only an additional term, the EOM's integral requires only an additional term to the specific kinetic energy, as shown in Eq (32). If Eq (32) is differentiated to check the integral, the second EOM of Eq (29) must be substituted to obtain the first EOM of Eq (29).

$$\varepsilon \equiv \frac{1}{2}(\dot{r}^2 + r^2\dot{\theta}^2) + \tau^* r \tag{32}$$

5.2 Radial Solution. The angular momentum constant in Eq (31) can be used in place of the angular speed in Eq (32) to provide a separable, first order EOM for the payload as shown in Eq (33).

$$
\begin{aligned}
dt &= r(-2\tau^{+}r^{3}+2\varepsilon r^{2}-h^{2})^{-1/2}\,dr \\
&\equiv \frac{\sqrt{2}}{2\sqrt{\tau^{+}}}\frac{r\,dr}{\sqrt{(\alpha-r)(r-\beta)(\delta-r)}}
\end{aligned}
\qquad \textbf{(33)}
$$

The three roots of the cubic have been defined in Eq (33) and can be evaluated as shown in Eq (34) (5:9).

$$
\begin{aligned}
0 &= y^{3}+py^{2}+qy+r \\
0 &= x^{3}+ax+b \qquad (y \equiv x-p/3) \\
a &= (3q-p^{2})/3 \qquad b = (2p^{3}-9pq+27r)/27 \\
A &\equiv (-b/2+(b^{2}/4+a^{3}/27)^{1/2})^{1/3} \qquad B \equiv -(b/2+(b^{2}/4+a^{3}/27)^{1/2})^{1/3} \\
x &= A+B, \quad -\left[(A+B)+(A-B)\sqrt{-3}\right]/2, \quad -\left[(A+B)-(A-B)\sqrt{-3}\right]/2
\end{aligned}
\qquad \textbf{(34)}
$$

One of these roots, δ, is negative while the other two, α and β, are positive (all are real). The two positive roots correspond to the apo-orbiter and peri-orbiter (maximum and minimum) radii of the payload, respectively (14:353). Conceptually, a payload reeled from a specific radial distance will accelerate under tension toward the orbiter to the peri-orbiter radius, then decelerate under the tension until it reaches the apo-orbiter radius. This cyclic motion about the orbiter under continuous tension is an open trajectory, since a specific radius won't occur after a full revolution.

Eq (33) is an elliptic integral and can generally be expressed in terms of the incomplete elliptic integrals of the first, second, and/or third kind. The integral transformation is performed with the radius-to-amplitude (r→ϕ) substitutions given in Eq (35) (14:353).

$$r \equiv \frac{\beta - m\delta\sin^2\phi}{1 - m\sin^2\phi 1} \qquad dr = \frac{m(\beta-\delta)}{\Delta(\phi)^4}\sin 2\phi \; d\phi \tag{35}$$

$$\textit{where} \qquad m \equiv (\alpha-\beta)/(\alpha-\delta) \qquad \Delta(\phi) \equiv \sqrt{1 - m\sin^2\phi}$$

Wiesel presents the transformed integral based on the incomplete elliptic integrals of the first and second kind. The initial and resultant integrals are shown in Eqs (36) through (38) (14:353). Eqs (39) and (40) are the incomplete elliptic integrals of the first and second kind, respectively (1:589). Both the Jacobi form (with x) and the Legendre form (with φ) in terms of the parameter, m, are presented. The "elliptic" terminology for the integrals refers to their use to calculate arc length of an ellipse (2:73). Since Eq (37) is a transcendental equation for amplitude (and radial position) as a function of time, it is typically solved with an iterative technique. The amplitude/radial position rates are related as shown for the differentials in Eq (36), and can be used during a Newton-Rhapson iteration. This method of solution is faster relative to direct integration of the EOMs of Eqs (27) and (28) (15).

$$\int_{t_\beta}^{t} dt = \int_{\beta}^{r} \frac{\sqrt{2}}{2\sqrt{\tau^*}} \frac{r\,dr}{\sqrt{(\alpha-r)(r-\beta)(\delta-r)}} \qquad [\alpha \geq r > \beta > 0 > \delta] \tag{36}$$

$$t - t_\beta = c_1 E(\phi|m) + c_2 \frac{\sin 2\phi}{\Delta(\phi)} + c_3 F(\phi|m) \tag{37}$$

$$c_1 \equiv \frac{\sqrt{2}(\beta-\delta)}{\sqrt{\tau^*(\alpha-\delta)}\,(1-m)} \qquad c_2 \equiv -\frac{m}{2} c_1 \qquad c_3 \equiv \frac{\sqrt{2}\,\delta}{\sqrt{\tau^*(\alpha-\delta)}} \tag{38}$$

$$F(\varphi|m) \equiv \int_0^{\varphi} \frac{d\varphi}{\sqrt{1 - msin^2\varphi}} = \int_0^{x} \frac{dx}{\sqrt{(1-x^2)(1-mx^2)}} \qquad (x \equiv \sin\varphi) \qquad \textbf{(39)}$$

$$E(\varphi|m) \equiv \int_0^{\varphi} \sqrt{1 - msin^2\varphi}\; d\varphi = \int_0^{x} \frac{\sqrt{1-mx^2}}{\sqrt{1-x^2}} dx \qquad (x \equiv \sin\varphi) \qquad \textbf{(40)}$$

5.3 Angular Solution. As with the radial solution, a separable differential equation for θ can be obtained by substituting Eq (31) for r in Eq (32). After separation, the differential equation can be transformed using the parameters in Eq (35) to obtain Eq (41). In this equation the reference angle corresponds to the peri-orbiter angle in the same manner as the reference time in Eq (36). The incomplete elliptic integral of the third kind is shown in Eq (42) (1:590) with the characteristic, n, which is not applicable to the incomplete elliptic integrals of the first and second kind.

$$\theta - \theta_\beta = \frac{\sqrt{2}}{\sqrt{\tau^*}\,\sqrt{\alpha-\delta}\;\beta\delta}\left[\beta F(\phi|m) + (\delta-\beta)\,\Pi(\delta m/\beta;\phi|m)\right] \qquad \textbf{(41)}$$

$$\begin{aligned} \Pi(n;\varphi|m) &\equiv \int_o^{\varphi} \frac{d\varphi}{(1 - nsin^2\varphi)\sqrt{1 - msin^2\varphi)}} \\ &= \int_o^{x} \frac{dx}{(1-nx^2)\sqrt{(1-x^2)(1-mx^2)}} \qquad (x \equiv \sin\varphi) \end{aligned} \qquad \textbf{(42)}$$

5.4 Full Arc Computation. With the full tension orbit modelled, computation of a portion of the orbit, or full arc is possible. However, an actual full arc never begins at the peri-orbiter radius as was assumed for the lower integration terminal in Eqs (33) and (41). For the operational case of a free arc deployment from an orbiter followed by a full arc, the initial radius for the full arc is the radius at the time of the switch to tension. Thus, the switching time does not correspond to the reference (apo-orbiter) time of Eqs (33) and (41). The actual peri-orbiter time can be obtained by substituting the switching time and switching radius/amplitude in Eq (37). Likewise, the peri-orbiter angular position in Eq (41) can be obtained.

5.5 Elliptic Integral Evaluation. To compute the desired time or angular position from Eqs (33) and (41), the values of the incomplete elliptic integrals for the specific conditions are required. Essentially, these integrals are complications of the basic trigonometric functions. Eq (43) shows that Eqs (39), (40), and (42) reduce to trigonometric functions when the amplitude is the only non-unity argument.

$$\begin{aligned} F(\varphi|1) &= \int_0^{\varphi} \frac{d\varphi}{\cos^2\varphi} = \tan\varphi \\ E(\varphi|1) &= \int_0^{\varphi} \cos\varphi \; d\varphi = \sin\varphi \\ \Pi(1;\varphi|1) &= \int_0^{\varphi} \frac{d\varphi}{\cos^3\varphi} = \sec^3\varphi \end{aligned} \qquad \mathbf{(43)}$$

Unlike basic trigonometric functions, the general values of the incomplete elliptic integrals are usually available only in tables and not as calculator or computer functions. However, Gauss's method of the arithmetic-geometric mean can be used to evaluate the integrals (2:72). The computation is based on Landen's transformation which is performed recursively via an arithmetic mean, a_n; a geometric mean, b_n; and a difference mean, c_n; using specific initial values for each. However, the routine provides the complete elliptic integral values of the first and second kinds (K(m) and E(m), respectively), which are the corresponding incomplete elliptic integrals evaluated when the amplitude is $\pi/2$. The arithmetic-geometric mean process is shown in Eq (44) (1:598).

$$\begin{array}{lll} a_1 = \frac{1}{2}(a_0 + b_0) & b_1 = (a_0 b_0)^{1/2} & c_1 = \frac{1}{2}(a_0 - b_0) \\ a_2 = \frac{1}{2}(a_1 + b_1) & b_2 = (a_1 b_1)^{1/2} & c_2 = \frac{1}{2}(a_1 - b_1) \\ \vdots & \vdots & \vdots \\ a_N = \frac{1}{2}(a_{N-1} + b_{N-1}) & b_N = (a_{N-1} b_{N-1})^{1/2} & c_N = \frac{1}{2}(a_{N-1} - b_{N-1}) \end{array} \tag{44}$$

This process continues until the arithmetic mean equals the geometric mean to the desired accuracy.

The complete elliptic integrals of the first and second kind are computed as shown in Eq (45) (1:598,599). The modular angle, α, defined in this equation represents a different quantity than the apo-orbiter radius defined earlier.

$$\begin{aligned} K(a_0,b_0,c_0) &= \frac{1}{2a_N} = K(a_N) \\ K(m) &= K\left(1,\sqrt{1-m},\sqrt{m}\right) \equiv K(1,\cos\alpha,\sin\alpha) = K(\alpha) \\ E(m) &= K(m)\left[1 - \frac{1}{2}\left(c_0^2 + \sum_{n=1}^{N} 2c_n^2\right)\right] = E(\alpha) \end{aligned} \tag{45}$$

To obtain the value of an incomplete elliptic integral, an additional iteration (the descending Landen transformation) is required using the amplitude. The iteration and Jacobi's zeta function are shown in Eq (46), while the incomplete elliptic integral values (first and second kind) are shown in Eq (47) (1:699). Eq (47) demonstrates the use of two delimiters, | and \, which are used with the parameter and modular angle, respectively. Occasionally, notation with a comma as the delimiter and the modulus, $k=m^2$, in place of the parameter is used (2:69).

$$\begin{aligned} \tan(\varphi_{n+1}-\varphi_n) &= (b_n/a_n)\tan\varphi_n, \quad \varphi_0 = \varphi \\ \varphi_n &= \tan^{-1}\left[(b_{n-1}/a_{n-1})\tan\varphi_{n-1}\right]+\varphi_{n-1} \\ Z(\varphi|m) &= \sum_{n=1}^{N} c_n \sin\varphi_n \end{aligned} \tag{46}$$

$$\begin{aligned} F(\varphi|m) &= \varphi_N/(2^N a_N) = F(\varphi\backslash\alpha) \\ E(\varphi|m) &= Z(\varphi|m)+[E(m)/F(m)]F(\varphi|m) = E(\varphi\backslash\alpha) \end{aligned} \tag{47}$$

Computation of the incomplete elliptic integral of the third kind is similar, but has exclusive cases for varying ranges of the characteristic, $n=\delta m/\beta$. The characteristic is always negative for the tether since it's based on the negative root, δ; the positive parameter, m; and the positive peri-orbiter radius, β. A negative characteristic is Abramowitz and Stegun case four (iv) for the integral, which is evaluated as shown in Eq (48) (1:590,591,599,600). The case four incomplete elliptic integral of the third kind is a function of the case three integral, which is evaluated as shown in Eq (49).

$$
\begin{aligned}
N &= (\sin^2\alpha - n)(1-n)^{-1}\\
p_2 &= [-n(1-n)^{-1}(\sin^2\alpha - n)]^{1/2}\\
\Pi(n;\varphi\backslash\alpha) &= \Big\{[(1-N)(1-N^{-1}\sin^2\alpha)]^{1/2}\Pi_{iii}(N;\varphi\backslash\alpha)\\
&\quad + p_2^{-1}\sin^2\alpha F(\varphi\backslash\alpha)\\
&\quad + \tan^{-1}[(1/2)p_2 sin2\varphi/\Delta(\varphi)]\Big\}\Big/\\
&\quad [(1-n)(1-n^{-1}\sin^2\alpha)]^{1/2}
\end{aligned}
\tag{48}
$$

$$
\begin{aligned}
\varepsilon &= \sin^{-1}[(1-N)/\cos^2\alpha]^{1/2} \qquad 0\le\varepsilon\le(\pi/2)\\
\beta &= (1/2)\pi F(\varepsilon\pi/2-\alpha)/K(\alpha)\\
q &= \exp\left[\frac{-\pi K(1-m)}{K(m)}\right] \qquad (\mathit{Nome})\\
\nu &= (1/2)\pi F(\varphi\backslash\alpha)/K(\alpha)\\
\delta_2 &= [N(1-N)^{-1}(N-\sin^2\alpha)^{-1}]^{1/2}\\
\lambda &= \tan^{-1}(\tanh\beta\tan\nu)\\
&\quad +2\sum_{s=1}^{\infty}(-1)^{s-1}s^{-1}q^{2s}(1-q^{2s})^{-1}\sin 2s\nu\sinh 2s\beta\\
\mu &= \left[\sum_{s=1}^{\infty} sq^{s^2}\sinh 2s\beta\right]\left[1+2\sum_{s=1}^{\infty} q^{s^2}\cosh 2s\beta\right]\\
\Pi_{iii}(N;\varphi\backslash\alpha) &= \delta_2(\lambda - 4\mu\nu)
\end{aligned}
\tag{49}
$$

In Eqs (48) and (49), N is an additional functional parameter unrelated to the final iteration index of Eqs (44), (45), and (46); while ε, β, and μ in Eq (49) are also unrelated to the previous physical parameters.

6 Optimization

Propulsion of a payload from an initial orbit to a final orbit can be optimized for maximum or minimum specific energy of the final orbit. This type of optimization results in a corresponding orbit size (semi-major axis) with a unique, but unspecified shape (eccentricity) during the optimization. Regardless of whether maximum or minimum specific energy is desired, the optimum condition is maximum change in the payload's specific energy from the initial value.

6.1 Parameter Considerations. The free arc and full arc solutions are functions of the initial orbit, the mission, and the physical variables as shown in Table 3.1. The initial orbit variables are essentially the CM position and velocity relative to the earth, while the mission variables are the initial state vector (payload position and velocity relative to the orbiter) and the sequence and duration of the free and full arcs used. The physical variables are the payload, orbiter, and planet masses and the tether tension limit.

Table 3.1 - Tether Variables

Orbit	Mission	Physical
R_0, V_0, Ω, P	θ_0, v_0, t_i, t_f	μ, m_1, m_2, τ^+

The impact of a particular variable depends on the relative size of the force that varies relative to the variable. Clearly, greater tether accelerations allow greater payload speeds and energy changes. Additionally, the planet mass and initial orbit are indicators of the gravity forces, with more massive planets and lower orbits having higher gravity and rotational effects when other parameters (like tether tension) are considered the same. Since these initial orbit and physical variables provide continually increasing or decreasing payload energy (depending on their variation), they are not used for optimization.

Most of the mission parameters have non-continual variations for payload orbital energy. First, the initial conditions can be reduced to an initial ejection angle and speed since the payload location is known (usually the same as the orbiter). In this case, the ejection speed is another continual variable, not viable for optimization, and therefore considered constant. However, the deployment or ejection angle will have a periodic affect on payload orbital energy. For example, a specific angle may increase payload energy, and variation from the specific angle will increase or decrease the final orbital energy. If it is an optimum deployment angle, variation will decrease the energy regardless of the direction of the variation. Likewise, an angle in the opposite direction will essentially decrease orbital energy and variations from it (if it's optimum) will increase energy. Thus, for the full range of ejection angles (360 degrees), at least two optimum angles exist.

The sequence and duration of the free and full arcs also affect the final payload energy. Clearly, the full arc's acceleration changes the energy during reel-in. However, following ejection from the orbiter, a free arc is used to provide separation. Thus, greater free arc durations allow greater full arc acceleration periods. A fixed mission duration is useful for considering this relationship. For a single cycle of a free arc followed by a full arc, the mission duration is from deployment on a free arc until the full arc is completed. Increasing free arc durations reduce the full arc period for a given mission duration. Thus, an optimum free arc duration exists for the single cycle case.

This duration describes an optimum switching time to activate tether tension and switch from the free arc to a full arc. Although mission duration can be varied, as well, it provides continually increasing energy changes (in most cases). Thus, mission duration isn't useful as an optimization parameter unless special conditions are applied.

Alternately, multiple cycles of free and full arcs can be used, providing additional switching times. For a double cycle (free arc, full arc, free arc, full arc) of a specific mission duration, the individual arc durations will be smaller than those of the single cycle case and the payload will remain in closer proximity to the orbiter. This allows shorter tether lengths for a specific mission duration. Although additional cycles introduce more switching times and increase the dimensionality, they can be used to examine lower payload separations. Additionally, a similar energy change should be obtainable since the duration of the payload acceleration by the tether is comparable to the single cycle case (although separated across two full arcs).

Regardless of the number of cycles, the optimum switching time will result in a case where a full arc terminates about a point with no reel-in capability remaining. This point occurs when the tether speed is zero and the payload is moving only tangentially relative to the orbiter. For optimization of energy (minimum or maximum) and for a specific conceptual trajectory, the affect of tether acceleration with respect to the CM velocity and the potential energy is complex. For example, the velocity (relative to the orbiter) of a payload moving conceptually toward a planet under tension is essentially perpendicular to the CM velocity and the potential energy is decreasing. At some point prior to the tangent condition, the kinetic energy, which is increasing due to the tether tension, will be increasing at the same rate as the potential energy is decreasing, resulting in maximum energy. On the other hand, trajectories with different directions and/or a mission times may optimize with the full arc ending after the tangent condition. Although this decreases payload speed relative to the orbiter, the post-tangent condition tension could change the velocity to a favorable direction along or opposite the CM orbital velocity (15).

6.2 Payload Energy Change Function. To achieve maximum propulsive capability, the specific energy function must be optimized. The function, Eq *(50), can be obtained from Eqs (9) and (12). In Eq (50), the payload mass* is generally negligible relative to the orbiter mass, allowing the mass ratio coefficients to be dropped. Also, expansion of the potential energy to second order eliminates negligible position terms.

Energy is optimized when the change in payload energy from ejection to mission completion is maximum or minimum (increased or decreased as much as possible). For deployment from the orbiter, the initial coordinates are zero. In most cases, the deployment speed is low relative to the final speed, and can be considered negligible. This results in a change in orbital energy as shown in Eq (51). If the deployment speed isn't negligible relative to the final speed, $(\xi_1)_f-(\xi_1)_i$ may be used for $\Delta\xi$.

$$\xi_1 \equiv \frac{E_1}{m_1} = \frac{T_1 + V_1}{m_1} = \frac{1}{2}\frac{m_2}{m_1 + m_2}\left((\dot{\rho} - \Omega\eta)^2 + (v_o + \dot{\eta} + \Omega\rho)^2\right) - \frac{\mu}{\sqrt{\left(R_o + \rho\frac{m_2}{m_1 + m_2}\right)^2 + \left(\eta\frac{m_2}{m_1 + m_2}\right)^2}} \tag{50}$$

$$= \frac{1}{2}\left((\dot{\rho} - \Omega\eta)^2 + (v_o + \dot{n} + \Omega\rho)^2\right) - \frac{\mu}{R_o} + \frac{\mu\rho}{R_o^2} - \frac{\mu\rho^2}{R_o^3}$$

$$\Delta\xi = \frac{1}{2}(\dot{\rho} - \Omega\eta)^2 + v_{cm}(\eta + \Omega\rho) + \frac{1}{2}(\dot{\eta} + \Omega\rho)^2 + \frac{\mu\rho}{R_o} - \frac{\mu\rho^2}{R_o^3} \tag{51}$$

6.3 Safe Separation Conditions. Regardless of the number of cycles of free and full arcs, shorter durations keep the payload in closer orbiter proximity and increase the likelihood of undesirable consequences. To maintain safe separation, optimization of energy must be performed while continually maintaining the payload position greater than a safety radius. However, this condition doesn't apply to the first free arc since the payload is considered safe during ejection from the orbiter and throughout the first free arc (no subsequent close passage). The radius and radial rate (tangent) conditions for safe separation are shown in Eq (52). Safe separation (radius) is r_{safe}, while minimum separation (radius) is r_{tan}.

Eq (52) provides two constraints for optimization. In general, constraints can be expressed as a series of the optimization parameters. A first order model is shown in Eq (53).

$$\Delta r \equiv r_{\tan} - r_{safe} = 0 \qquad \dot{r}_{\tan} = 0 \tag{52}$$

$$0 = \vec{C} \approx \vec{C}_o + \left[\frac{\partial \vec{C}}{\partial \vec{S}}\right]_o d\vec{S} \quad \therefore \quad d\vec{S}_{(n+1)} = \left[\frac{\partial \vec{C}}{\partial \vec{S}}\right]_n^{-1} \vec{C}_n \tag{53}$$

6.4 Pertinent Optimization Cases. Various optimizations of free and full arcs can be used, some of which are shown in Table 3.2. In this table, the cycles term refers to the number of free arcs and full arcs. For example, 1.5 cycles represent the conceptual operation of a free arc followed by a full arc and a subsequent free arc. The operation is conceptual since the payload may be released from the tether following the full arc. The free arc is computed for safe separation, only. The switching times, t_i, represent the chronological delimiting points between arcs. However, the duration of an arc is variable, and may optimize to zero. This is occasionally the case with the second free arc. Table 3.3 depicts the chronological sequence of full and free arcs for the cases shown in Table 3.2, except for case E which is double cycle of case A. The negative and positive superscripts in Table 3.3 indicate whether the end of the full arc conceptually occurs before or after the tangent condition.

Case A optimizes energy change for a specific mission/final time, t_f. The final state vector provides an indicator of whether the payload has passed the tangent condition. The radial rate is negative before the tangent condition and positive after the tangent condition.

Table 3.2 - Conceptual Optimization Cases

CASE & CYCLES	OPERATION	CONSTRAINT VECTOR - $\bar{c}$	PARAMETER VECTOR - $\bar{s}$	COMMENT
A 1.0	Optimizes.	$\begin{bmatrix} \partial(\Delta\xi)/\partial\theta_0 \\ \partial(\Delta\xi)/\partial t_1 \end{bmatrix}$ **(54)**	$\begin{bmatrix} \theta_o \\ t_1 \end{bmatrix}$ **(55)**	(14:354)
B 1.0	Optimizes.	$\begin{bmatrix} \partial(\Delta\xi)/\partial\theta_o \\ \partial(\Delta\xi)/\partial t_1 \\ \partial(\Delta\xi)/\partial t_f \end{bmatrix}$ **(56)**	$\begin{bmatrix} \theta_o \\ t_1 \\ t_f \end{bmatrix}$ **(57)**	Invalid, since t_f variations will continue to change ξ_f if θ_o and t_1 are variable.
C 1.5	Optimizes.	$\begin{bmatrix} \partial(\Delta\xi)/\partial\theta_o \\ \partial(\Delta\xi)/\partial t_1 \\ \partial(\Delta\xi)/\partial t_2 \end{bmatrix}$ **(58)**	$\begin{bmatrix} \theta_o \\ t_1 \\ t_2 \end{bmatrix}$ **(59)**	Same as case B since second free arc has no $\Delta\xi$.
D 1.5	Optimizes and determines mission time for the separation margin.	$\begin{bmatrix} \partial(\Delta\xi)/\partial\theta_o \\ \partial(\Delta\xi)/\partial t_1 \\ r_{\tan}-r_{safe} \end{bmatrix}$ **(60)**	$\begin{bmatrix} \theta_o \\ t_1 \\ t_f \end{bmatrix}$ **(61)**	Same as case A if safe separation radii are mapped.
E 2.0	Optimizes.	$\begin{bmatrix} \partial(\Delta\xi)/\partial\theta_o \\ \partial(\Delta\xi)/\partial t_1 \\ \partial(\Delta\xi)/\partial t_2 \\ \partial(\Delta\xi)/\partial t_3 \end{bmatrix}$ **(62)**	$\begin{bmatrix} \theta_o \\ t_1 \\ t_2 \\ t_3 \end{bmatrix}$ **(63)**	Similar to case A; closer separations.

Table 3.3 - Chronological Sequence of Conceptual Cases

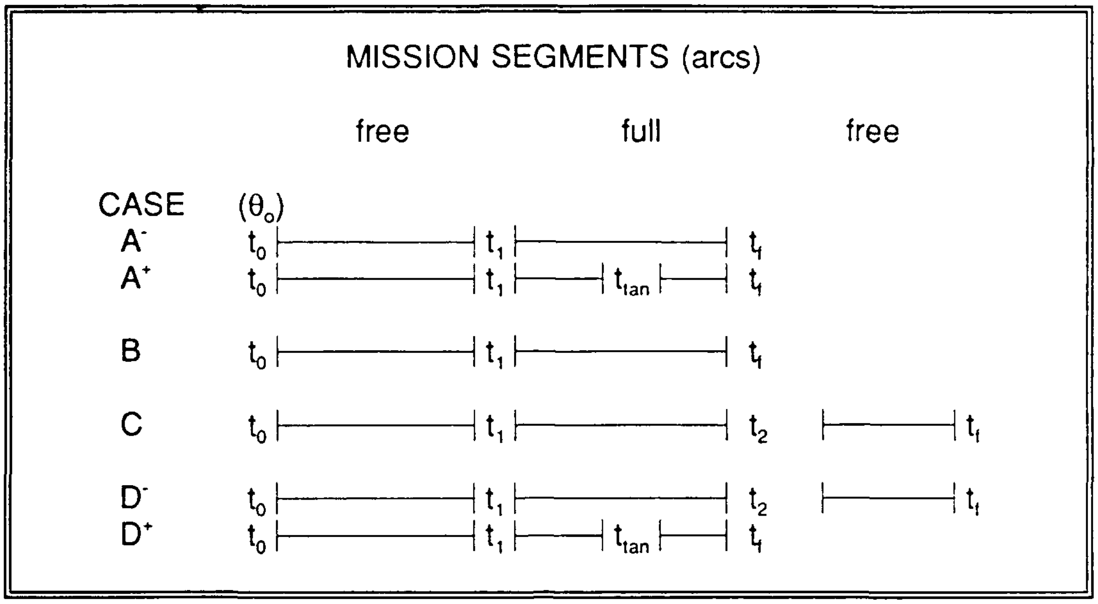

Eq (54) calculates the radial rate from the state vector. If the mission ends after the tangent condition has been passed (as indicated by a positive superscript in Table 3.3), the peri-orbiter radius of the full arc is the separation distance. However, if the mission ends before the tangent condition (as indicated by a negative superscript), a subsequent free arc must be used to calculate the time of the tangent condition and the separation. Also, case A is optimized for a family of trajectories using varying values of the final time. Thus, the final time can be considered a mapping parameter and separation for each final time can be determined.

$$\dot{r} = \frac{\vec{r}\cdot\vec{v}}{\sqrt{\vec{r}\cdot\vec{r}}} \qquad \vec{X} \equiv \{\vec{r}^{T} \;\; \vec{v}\} = \{[\rho \;\; \eta] \;\; [\dot{\rho} \;\; \dot{\eta}]\} \tag{64}$$

Both case B and case C are conceptually invalid since a greater final time (or end-of-full-arc time) allows greater energy changes. On the other hand, an optimum energy does exist at an optimum final time for a specific deployment angle or switching time. This would be a revision of case A with the final time substituted for the specific deployment angle or switching time. This could be useful for specifying an orbit shape with a specified deployment angle since the final position and velocity would be specific for the optimized switching and final times. However, since cases B and C allow deployment angle and switching time to optimally vary along with the final time, no zero can be expected for the energy change function. This renders cases B and C undesirable for optimization.

Case D optimizes in the same manner as case A, but implicitly determines the mission, or final time, t_f, for a desired separation margin, $\Delta r = r_{tan} - r_{safe}$. In this case, the results are the same as case A with the final time and separation margins being interchanged as independent and dependant optimization parameters.

Case E is for a double cycle and is similar to case A. It allows determination of optimum deployment angle and switching times for a given final time, as well. Separation distance can be calculated for the two tangent conditions and examined. For any final time, the separation distance is lower than that of case A. However, this disadvantage is offset by the shorter tether length required.

6.5 Iterations. Iteration during the optimization is required at varying points, or levels. First, a final time iteration is essential in all valid cases of Table 3.2, except case D. At the lowest level, the arithmetic-geometric mean is required to determine the complete elliptic integral of the first kind. Table 3.4 summarizes the various iterations required for determining a family of trajectories.

Table 3.4 - Required Optimization Iterations.

DESCRIPTION	PARAMETER(S)	EQUATION
Mapping	t_f	n/a
Optimization	θ_o, t_i	(53)
Derivative Calculation	$\partial^n c/\partial s^n$	(69)
Nome series	$\Pi(n;\varphi\|m)$	(49)
Descending Landen Transformation	$F(\varphi\|m), E(\varphi\|m)$	(46)
Arithmetic-Geometric Mean	a_n, b_n, c_n, φ_n $K(m), E(m)$	(44)

The primary iteration of the mission time as a mapping parameter covers a finite time segment. A segment near the CM orbital period is appropriate. Since small mission times are operationally unworthy because their minimum separation can be unsafe, a useful lower limit follows as the mission time that gives a trajectory with the lowest acceptable minimum separation distance. In the same fashion, large mission times may have corresponding always-safe tangent conditions, which would allow a segment upper limit to be defined. In the absence of such a condition, the CM orbital period can be used as an upper limit.

For any mission time, a seed value for each switching time is required. Switching times can be estimated using a rectilinear acceleration model as shown in Eq (65). This model assumes no gravity or rotational terms, only tether acceleration; and is especially applicable for short mission durations. The models for single cycle and double cycles are shown in Eqs (66) and (67), respectively. For both cases, this occurs when the payload is accelerated back to the r_0 point. Both cases require a t_2 value, while the double cycle case requires a t_4 value, as well. Also, a desirable seed for the deployment angle is not modelled and must be assessed for use in the optimization.

$$\begin{aligned} r_{i+1} &= r_i + v_i(t_{i+1} - t_i) + a_i(t_{i+1} - t_i)^2/2 \\ r_1 &= r_0 + v_0(t_1 - t_0) && (\textit{free arcs: } a_i = 0) \\ r_2 &= r_1 + v_0(t_2 - t_1) \quad - \tau^*(t_2 - t_1)^2/2 && (\textit{full arcs: } a_i = -\tau^*) \end{aligned} \tag{65}$$

$$\begin{aligned} r_1 &= v_0(t_1 - t_0) = -v_0(t_2 - t_1) + \tau^*(t_2 - t_1)^2/2 && (r_0 = 0 = r_2) \\ \therefore \quad t_1 &= t_2 - \sqrt{2v_0(t_2 - t_0)/\tau^*} && (\textit{any single cycle}) \\ \textit{and } v_2 &= \partial r_2/\partial t_2 = v_0 - \tau^*(t_2 - t_1) = v_0 - \sqrt{2v_0\tau^*(t_2 - t_0)} \end{aligned} \tag{66}$$

$$t_3 = t_4 - \sqrt{2(-v_2)(t_4 - t_2)/\tau^*} \quad (\textit{for the second cycle}) \tag{67}$$

While mapping the trajectories for numerous mission times, a function estimator can be used to estimate the best seed values for the next mission time in the mapping iteration when several previous trajectories are known. Aitken's Iteration Method provides this capability (1:879). However, care must be used while mapping the desired mission time segment. Since more than one optimum deployment angle exists for a desired mission time; the initial, or seed, deployment angle in the optimization determines which optimum deployment angle is obtained. This lock-on feature of the optimization iteration requires that different seed deployment angle segments be mapped to the desired degree.

During the optimization iteration, various derivatives are required. As a complete example, those required for case D are shown in Eq (68). Derivatives for the other cases are nearly identical.

$$\left[\frac{\partial \vec{c}}{\partial \vec{s}}\right] = \left[\frac{\partial\left\{\dfrac{\partial(\Delta\xi)}{\partial\theta_o} \quad \dfrac{\partial(\Delta\xi)}{\partial t_1} \quad \Delta r\right\}}{\partial(\theta_o \quad t_1 \quad t_f)}\right] = \begin{bmatrix} \dfrac{\partial^2(\Delta\xi)}{\partial\theta_o^2} & \dfrac{\partial^2(\Delta\xi)}{\partial\theta_o\partial t_1} & \dfrac{\partial^2(\Delta\xi)}{\partial\theta_o\partial t_f} \\ \dfrac{\partial^2(\Delta\xi)}{\partial t_1\partial\theta_o} & \dfrac{\partial^2(\Delta\xi)}{\partial t_1^2} & \dfrac{\partial^2(\Delta\xi)}{\partial t_1\partial t_f} \\ \dfrac{\partial(\Delta r)}{\partial\theta_o} & \dfrac{\partial(\Delta r)}{\partial t_1} & \dfrac{\partial(\Delta r)}{\partial t_f} \end{bmatrix} \tag{68}$$

Both the first and second order derivative values are computed numerically. The first order derivatives can be based on four equally spaced values of the desired constraint for each optimization parameter. For example, the first order partial derivative in row three, column one of Eq (68) would use $r_{\tan}$ values at the desired θ_o, two slightly higher θ_o values, and a slightly lower θ_o (all separated by equal amounts, $\delta\theta_o$. Essentially, these four points allow the derivative to be calculated like an average speed using four points rather than the usual two points. Any first order derivative can be calculated from the appropriate four points using Eq (69), where f is the desired constraint (range rate in the example) (1:883). Second order derivatives can be calculated using a three or seven point scheme over two optimization parameters as shown in Eqs (70) and (71) (1:884). In Eqs (70) and (71), $f_{i,j}$ represents the function evaluated as $f(x+i\delta x, y+j\delta y)$.

$$(\partial f/\partial x)_{0,0} = (-2f_{-1,0} - 3f_{0,0} + 6f_{1,0} - f_{2,0})/(6\delta x) \tag{69}$$

$$(\partial^2 f/\partial x^2)_{0,0} = (f_{-1,0} - 2f_{0,0} + f_{1,0})/\delta x^2 \tag{70}$$

$$\left(\frac{\partial^2 f}{\partial x \partial y}\right)_{0,0} = -(f_{1,0} + f_{-1,0} + f_{0,1} + f_{0,-1} - 2f_{0,0} - f_{1,1} - f_{-1,-1})/(2\delta x\delta y) \tag{71}$$

7 Summary

With the closed solution to the free arc and equations for the full arc available, the nested iterations can be used to optimize the families of trajectories for various seed values. The free arc is simply the relative motion of two orbiting bodies, while the full arc propels the payload toward the orbiter and is modelled with elliptical integrals. Of interest for a particular mission time are the deployment angles, the switching times, the trajectories, the resultant payload orbit, tether length, and separation.

IV Results

To investigate safe separation, tethered payload trajectories are determined using the computation method described in Chapter III. Trajectories for a nominal earth orbit are preferred, and require specification of numerous parameter values. These values are shown in Table 4.1.

Table 4.1 - Computational Parameter Values

PARAMETER	VALUE
ejection speed from orbiter, v_0	10 m/s
orbital linear speed, V_0	7740.604 m/s
orbital distance, R_0	6652550 m
earth's gravitational parameter, μ	3.986012×10^{14} m^3/s^2
orbital angular speed, Ω	0.0011635 rad/s
tether acceleration, τ^+	2 m/s^2

Since the orbit is circular; V_0, R_0, and Ω are determined from the desired orbital period (90 min). This period, and the values for v_0 and τ^+, are selected to coincide with the previous reel-in tether study (14:355). Additionally, the numerical derivatives are calculated using various δx and δy values. A small variation is chosen, ε=0.001, and determines $\delta\theta=\varepsilon$ and $\delta t_1=\varepsilon t_1$ for the single cycle mission (free arc deployment followed by a full arc). Finally, the optimization is performed until the ratios $(d\theta_0/\theta_0)_{(n+1)}$ and $(dt_1/t_1)_{(n+1)}$ of Eq (53) are below a tolerance value for acceptable accuracy, 0.000001.

1 Multiple Optimum Trajectories

For a mission time of 90 min (the orbital period), multiple optimum trajectories ($\Delta\xi=\xi_f-\xi_i$) for case A are determined by varying the seed angle from 0 to approximately 2π radians in 0.05 radian increments. For the seed t_1, the rectilinear model value was repeatedly used (86 min). The resultant optimum trajectory parameters are shown in Table 4.2.

Not all seed θ_0 values converged on an optimum trajectory. For cases where the seed θ_0 and t_1 values were distant from an optimum trajectory, an optimization iteration would increment the t_1 value to an illogical value below zero or above t_f. In these cases the iteration was halted and the next seed θ_0 was used. This extreme behavior can be seen for several iterations that converged on optimum θ_0 values distant of the seed θ_0 value. Also, several different seed values converged on the same optimum trajectory. Finally, the 16 trajectories can be considered only a sample of all optimum trajectories for a 90 min mission, since additional seed t_1 values give additional optimum trajectories.

However, deployment angles of 0 and π radians provide the trajectories with the overall minimum and maximum energy, as expected for a mission duration that corresponds to the orbital period. A rearward (0 radian) deployment results

Table 4.2 - Multiple Optimum Trajectory Parameters for a 90 min Mission

SEED θ_0, radians	OPTIMUM θ_0, radians	OPTIMUM t_1, s	RESULTANT PAYLOAD ORBIT SEMI-MAJOR AXIS, m
0.60	-5.07	272.644	6647022
0.70	-4.01	2623.570	6574237
0.75	-2.57	2443.369	6948796
0.90	-4.90	2777.363	6844445
1.25,1.35	0.00	4954.944	5616627
1.55	1.58	4668.038	6672039
1.85,1.90, 4.40,4.45	3.14	4958.679	8333062
2.10	0.58	2467.216	6381570
4.05	-4.02	1209.393	6673693
4.10	-0.62	560.166	6640568
4.15	-0.57	2440.299	6521849
4.25	-2.68	3422.825	7318718
5.05	6.28	4954.944	5616627
5.20	2.87	4125.832	5848244
5.50	4.20	2725.959	6921121
5.55	3.68	2182.964	6408833

in a smaller payload orbit (minimum energy); while the opposite deployment results in a larger payload orbit. The optimum switching time, t_1, is significantly different from the rectilinear seed because of the high mission duration.

For comparison with the 90 min mission, Table 4.3 shows the multiple optimum trajectories for a 9 min mission. In this case, the rectilinear seed for

Table 4.3 - Multiple Optimum Trajectory Parameters for a 9 min Mission

SEED θ_0; radians	OPTIMUM θ_0, radians	OPTIMUM t_1, s	SEMI-MAJOR AXIS, m
0.05	-2.25	145.328	6649700
0.15,2.00	4.01	311.805	6658176
0.20	0.86	311.811	6646888
1.70,2.85	4.01	188.154	6656036
1.75,2.20,5.15,6.00	0.86	311.811	6646888
1.80,1.85,1.90,1.95	4.03	400.367	6644999
2.05	4.02	235.669	6648129
2.10	4.07	34.016	6651764
2.25,2.30	2.55	468.034	6430793
2.75	4.02	235.669	6648129
2.80	4.03	145.328	6649700
3.00,4.85,5.20,5.95	0.88	235.683	6656934
3.20	0.87	188.154	6649027
3.35	4.03	400.367	6644999
3.70	-5.37	30.477	6651852
3.90	0.88	539.998	6641645
4.90,5.35	4.01	311.805	6658176
4.95,5.00,5.05,5.10	0.88	400.387	6660067
5.25,5.90	0.90	79.756	6650929
5.30,5.40	5.69	468.028	6894448

t_1 is 467 s, which is nearer the optimum t_1 (8 min) since the rotational and gravity-gradient terms have less impact for the shorter mission. This is also the likely cause for the increase in the number of optimum trajectories detected for the 0.05 radian search.

2 Single Cycle Trajectory Family

For the 9 min mission, the optimum deployment angle for minimum energy is 2.55 radians, which is nearly opposite that of the 90 min mission (0.00 radians). Using the 90 min mission as a baseline, optimum minimum energy trajectories were mapped from 90 min to 7.5 min mission times at 1.5 min intervals. The 9 min mission at the end of the mapping converged to the same trajectory determined during the angular search, as expected. This agreement provides additional confirmation that the minimum energy trajectories were determined. These trajectories are of interest since they provide the maximum energy to the orbiter. When considering the orbiter as the desirable recipient of energy, the payload can be considered a sub-payload while the orbiter is the true payload. Stationkeeping with expendable masses (discardable parts or contained trash) is the operational scenario for this case. Maximum trajectories for the orbiter depend on the ratio of the payload and orbiter masses, and can be assessed from the minimum energy payload trajectory, as mapped.

Of interest during the mapping was the final radial rate, which indicates if the tether is being reeled-in or payed-out at the end of the mission. Figure 4.1 diagrams the radial rate and numerous other parameters. Each parameter is normalized to its maximum value (shown in parenthesis) during the mapping.

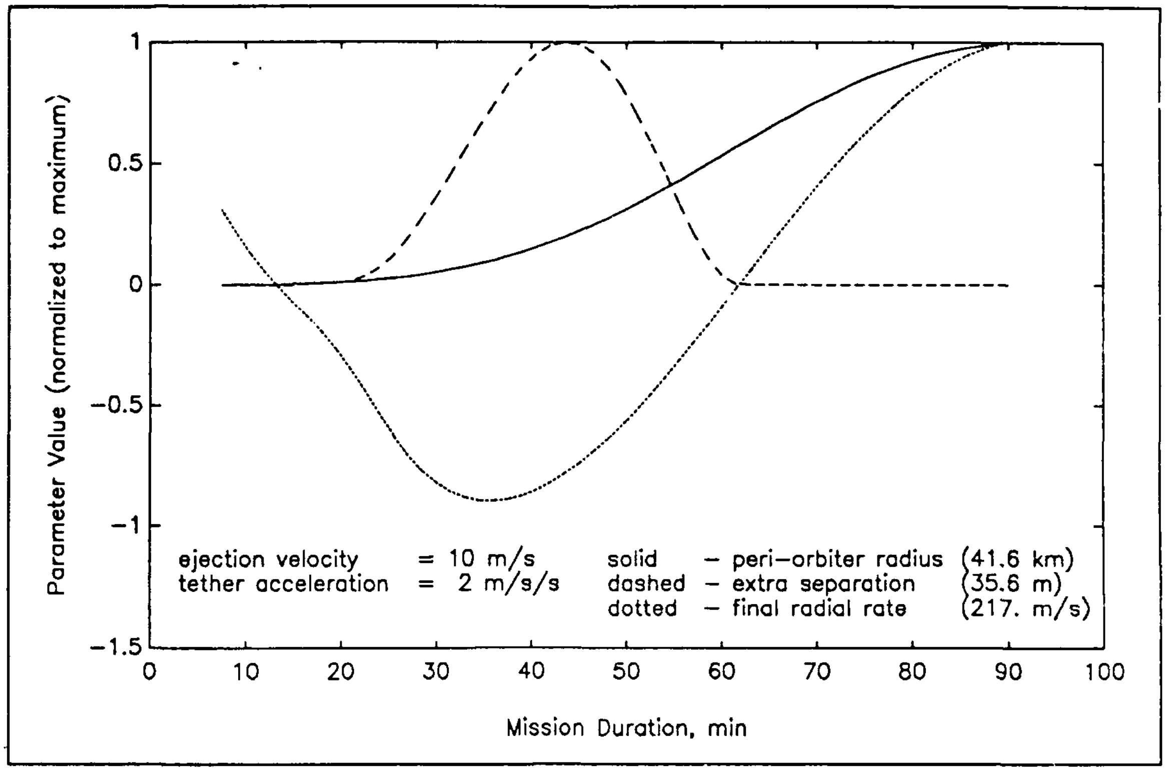

Figure 4.1 - Resultant Payload Parameters

During the mapping, approximately 5 optimization iterations were required. However, at the end of the mapping (22-7.5 min), up to approximately 25 iterations were required. The varied behavior of this portion of the radial rate function is the likely cause.

For two missions, 62 min and 13 min, the final radial rate is zero. This indicates that the final position is the location of minimum payload separation from the orbiter. The trajectories for these two missions are shown with the 90 min trajectory in Figure 4.2.

Since the final radial rate is negative during a portion of the mapping, these missions end prior to reaching the point of minimum separation. For these

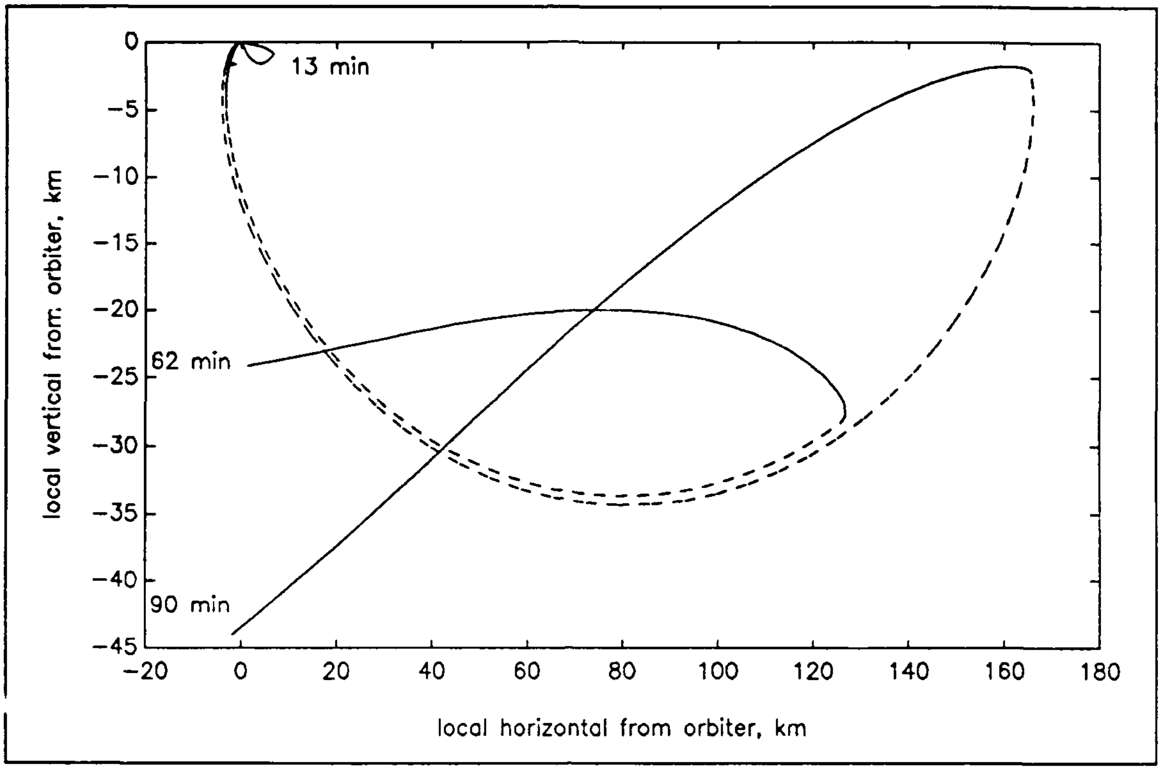

Figure 4.2 - Minimum Energy Trajectories

trajectories, the peri-orbiter radius fails to describe the minimum separation as it does for the missions with positive final radial rates. An additional free arc is conditionally calculated to determine the point of minimum separation (zero radial rate). In all cases, the minimum separation value is greater than the peri-orbiter radius for the full arc. However, the difference is small compared to the overall value for each mission. The extra separation above the peri-orbiter radius is shown in Figure 4.1, along with the peri-orbiter radius. The extra separation value is greatest for a 43.5 min mission, at 35.55 m above the peri-orbiter radius of 8134.83 m (0.44%).

As an estimate of propulsive capability, an impulsive velocity change value can be determined from the resultant payload orbit. Although the payload is released into its new orbit at a position away from the system CM, the new orbit is considered elliptically tangent to the initial circular orbit to obtain the estimate. Eq (72) is the model for the impulsive velocity change estimate, which uses the energy, or vis-viva, integral to determine the orbital velocity (2:116).

$$\begin{aligned} \Delta v &= |\overrightarrow{\Delta v}| = |\vec{v}_f - \vec{v}_i| \approx v_{model} - V_0 \\ &\equiv \sqrt{\mu(2/r_f - 1/a_f)} - V_0 \approx \sqrt{\mu(2/R_0 - 1/a_f)} - V_0 \end{aligned} \tag{1}$$

Figure 4.3 shows the velocity change capability of the tether for the various peri-orbiter values from Figure 4.1. Additionally, Figure 4.3 provides a tether length estimate and ratio of velocity change to tether length for the peri-orbiter values. The tether length estimate is based on the end of the free arc. Although the payload radius continues increasing after tension is initially applied, it quickly slows to zero and begins decreasing. The tether length serves as an indicator of overall tether mass, which is preferred to be as low as possible. Thus, the ratio of velocity change to length is an indicator of propulsive efficiency.

Figure 4.3 indicates that minimum separation (plotted as peri-orbiter radius) increases with higher velocity changes. Since higher velocity changes are typically desired, any choice above the a safe separation value is acceptable. Additionally, propulsive efficiency is nearly of direct proportion to the desired

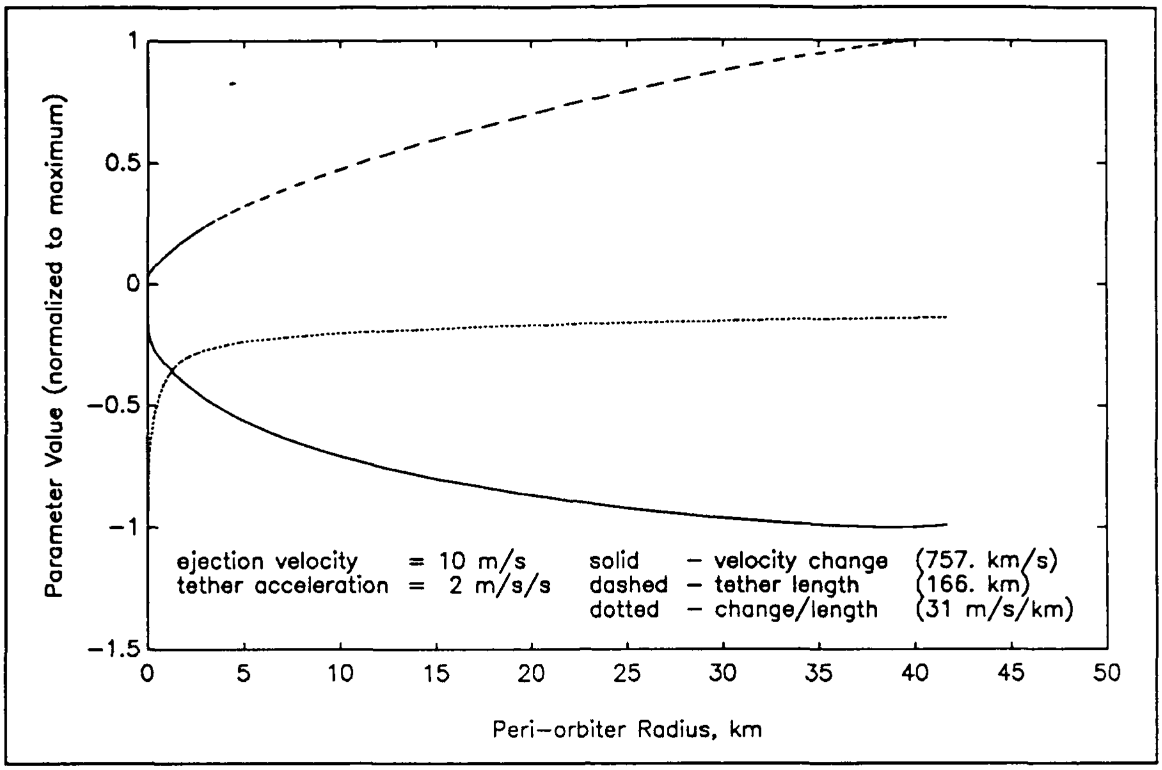

Figure 4.3 - Velocity Change and Tether Length

velocity change. The best efficiency occurs for 10 m of separation with -124 m/s velocity change for 4 km of tether length over a mission of 7.5 min. Unfortunately, t_1 became invalid during the mapping below a mission duration of 7.5 min, where better efficiencies probably exist. Although undesirable, this limitation doesn't impact the assessment of separation.

Since case A encompasses the range of minimum separation values for the family of trajectories, case D only serves as a means to determine a trajectory for a specific separation. For example, the 90 min mission has a large, 42 km minimum separation. Using the optimum trajectory for a 90 min mission as a seed, a minimum separation between 42 km and 30 km can be specified, and case D determines the trajectory for the specified separation. However, the function has a limited reach, and must have a suitable seed. The 90 min seed trajectory can reach a 30 km separation trajectory (68 min mission). Unfortunately, the reach decreases with mission time and prevents any feasible use of case D below approximately mission durations of 45 min. Thus, case A is preferred for determining separation.

3 Double Cycle Trajectory Family

Expansion to the double cycle case E followed the determination of case A trajectories. This case is of interest because of the shorter tether lengths and closer separations for a specific mission duration. Unfortunately, acceptable algorithmic behavior could not be accomplished for case E.

Initially, time estimates from the case A trajectory were concatenated for the 90 min mission. When the algorithm failed to lock-on or even track toward an optimum energy, the rectilinear seeds were used. However, small variations in seed values of θ_o, t_2, and t_4 consistently caused the payload energy change to switch polarity or in many cases, iterate to negative or out-of-sequence times. Tuning of ε for the derivative calculation was performed over a reasonable range (0.1 to 0.000001), followed by individual ξ tuning for each parameter. Although algorithmic tracking began to occur in some cases, optimum values were consistently by-passed unless the accuracy tolerance was set to a high value (0.1). The coarseness of this setting (1/10 radian or 1/10 of any of the times) provided lock-on, but for essentially any trajectory. This prevented automated location of the extreme optimum.

However, manual iterations and automated angular iterations for various seeds provided a sample of insightful trajectories. The parameters for these trajectories are shown in Table 4.4. The algorithm tracked to the first two trajectories of Table 4.4, but by-passed the optimum value. Occasionally this occurred with subsequent iterations that slowly moved from the optimum. However, just as often, the algorithm jumped to a distant trajectory. The momentary trajectory was one of a few to which the algorithm would infrequently jump. The positive (hyperbolic) energy is too extreme for realistic consideration, and is of little concern for separation. Finally, the 9 min trajectory parameters shown are one of the cases that optimized on one iteration because of a high tolerance setting.

4 Low Ejection Speed Family

As an alternative to a double cycle, a single cycle with a reduced ejection speed causes low separations. For a comparable tension acceleration, a low ejection speed decreases the amount of travel for a given free arc duration and reduces the subsequent distance for full arc acceleration. Thus, lower velocity change capability is expected in conjunction with the closer separation.

For a reduced ejection speed, the same tether acceleration is used to ensure similar dynamics during the full arc. A lower tether acceleration in

Table 4.4 - Case E Trajectory Parameters

Mission Duration, min	θ_0, radians	t_1, min	t_2, min	t_3, min	ξ_f, $m^2/s^2 \times 10^7$ ($\xi_i \approx -3.0\times10^7$)	Comment
90	5.45	3.47	7.77	34.66	-5.6535	By-passed
90	4.12	2.05	6.00	34.69	-0.0661	By-passed (after ≈700 previous iterations)
90	5.76	2.42	6.07	33.15	+3.3606 !	Momentary
9	2.40	0.15	0.42	5.00	-3.089	High ε

conjunction with the reduced ejection speed would tend toward higher minimum separations and limit the investigation.

The family of trajectories was mapped for v_0=1 m/s and τ^*=2 m/s^2 (the same as before). Table 4.5, Figure 4.4, and Figure 4.5 are the analogous data. With the lower ejection speed, the algorithm was able to continue longer, and map an additional trajectory (6 min). However, this was at the expense of increased optimization iterations during the loaded portion of the mapping, as before. Up to 93 iterations were required during mission durations of 31.5-15 min. Figure 4.4 shows this is the portion of the mapping where the final radial rate was increasing, as was the case for the higher ejection velocity. Also, the final radial rate begins decreasing with mission duration below 10.5 min.

Although the peri-orbiter radius trend is the same for this case, the value of the peri-orbiter radius is approximately 1/34 that for the higher ejection velocity

Table 4.5 - Optimum Trajectory Parameters for Low Speed Ejection

Mission Duration, min	OPTIMUM ϑ_0, radians	OPTIMUM t_1, s	RESULTANT PAYLOAD ORBIT SEMI-MAJOR AXIS, m
90	0.00	5270.999	6258677
90	3.16	5271.015	7114676
9	2.48	517.092	6577434
9	5.62	517.090	6729822

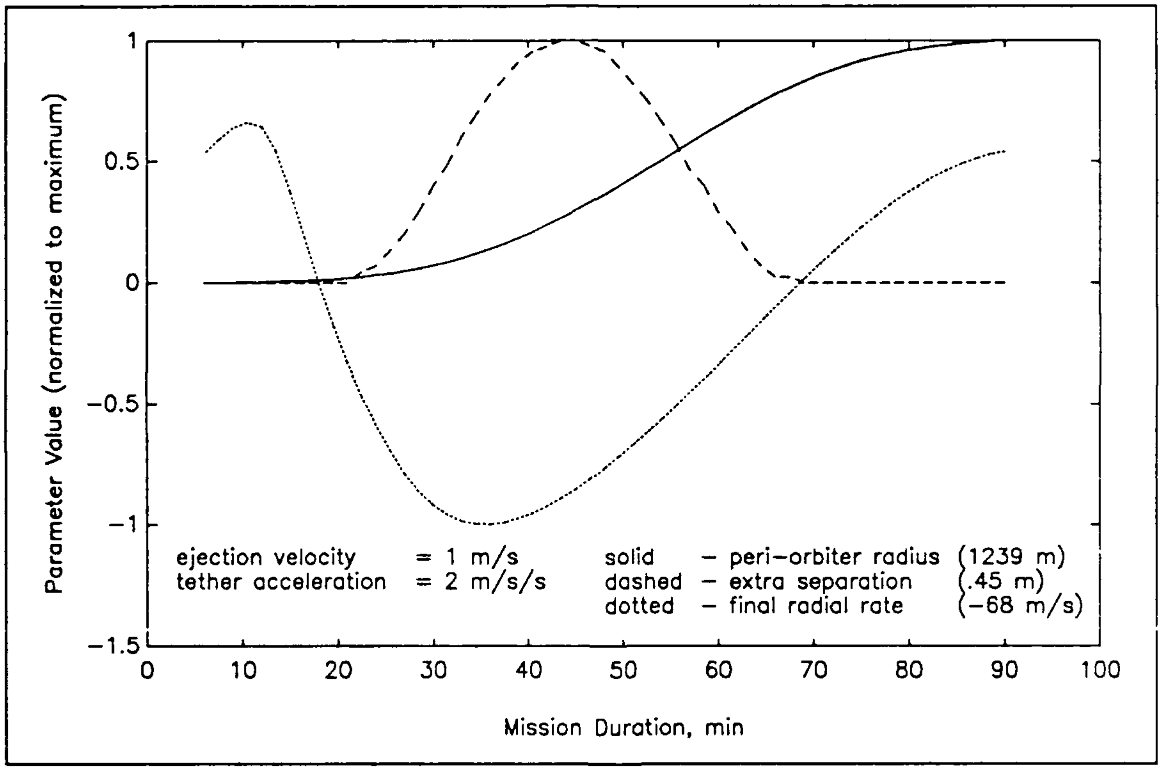

Figure 4.4 - Low Ejection Speed Parameters

situation. Additionally, the extra separation is smaller and more negligible. At its maximum value of 0.45 m for a mission duration of 43.5 min (again), it adds little to the peri-orbiter radius of 328.91 m (0.14%).

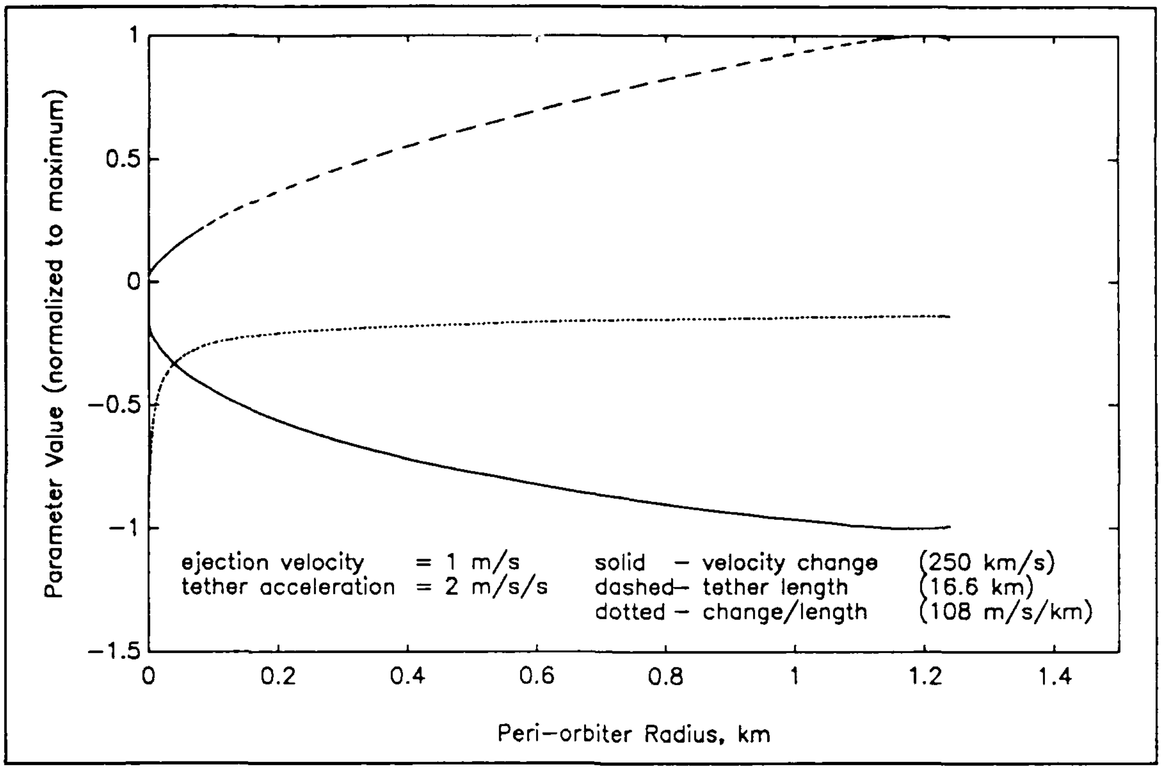

Figure 4.5 - Low Ejection Speed Velocity Change and Tether Length

5 Tether Length Comparison

As expected, the tether length is shorter for the lower ejection speed and the same mission duration. However, in addition to having the same trend, an unexpected correlation between tether length and velocity change is evident. For the maximum length with low ejection speed (16.6 km at a 79.5 min mission), the velocity change is -250 m/s. This is about the same (a bit more) than the velocity change for the same length tether with the high ejection velocity. Interpolating from the tabulated data for Figure 4.3, the corresponding high ejection velocity at 16.6 km is -238 m/s at a mission duration of 23.3 min. In addition to occurring at different mission durations, these two related trajectories have different separations. The high ejection speed peri-orbiter radius is 746 m, which differs from the low ejection speed peri-orbiter radius of 1197.87 m.

However, this is only an isolated case where the two velocity changes are equal. For a tether length of 4 km, the high ejection speed mission of 7.5 min had a -123 m/s change and a separation of 10.24 m, while the comparable low ejection speed mission of 31.5 min had a -65.60 m/s change and a separation of 103.09 m. Hence, a trade-off exists between velocity change and separation where the ejection velocity selects the desired trade-off. Figure 4.6 allows graphic comparison of the low speed trajectory with the small number of high speed trajectories that have the same tether lengths.

6 Summary

For stationkeeping, with an orbiter energy increase desired, the payload is propelled to a minimum energy orbit. The single cycle reel-in tether case indicates higher tether lengths allow greater energy and velocity changes for both the orbiter and payload, while increasing the minimum separation. Shorter tether lengths occur for the double cycle case, but optimization over the additional mission parameters failed to provide automated results. Alternately, a lower ejection speed causes closer separations; but at the expense of propulsion capability.

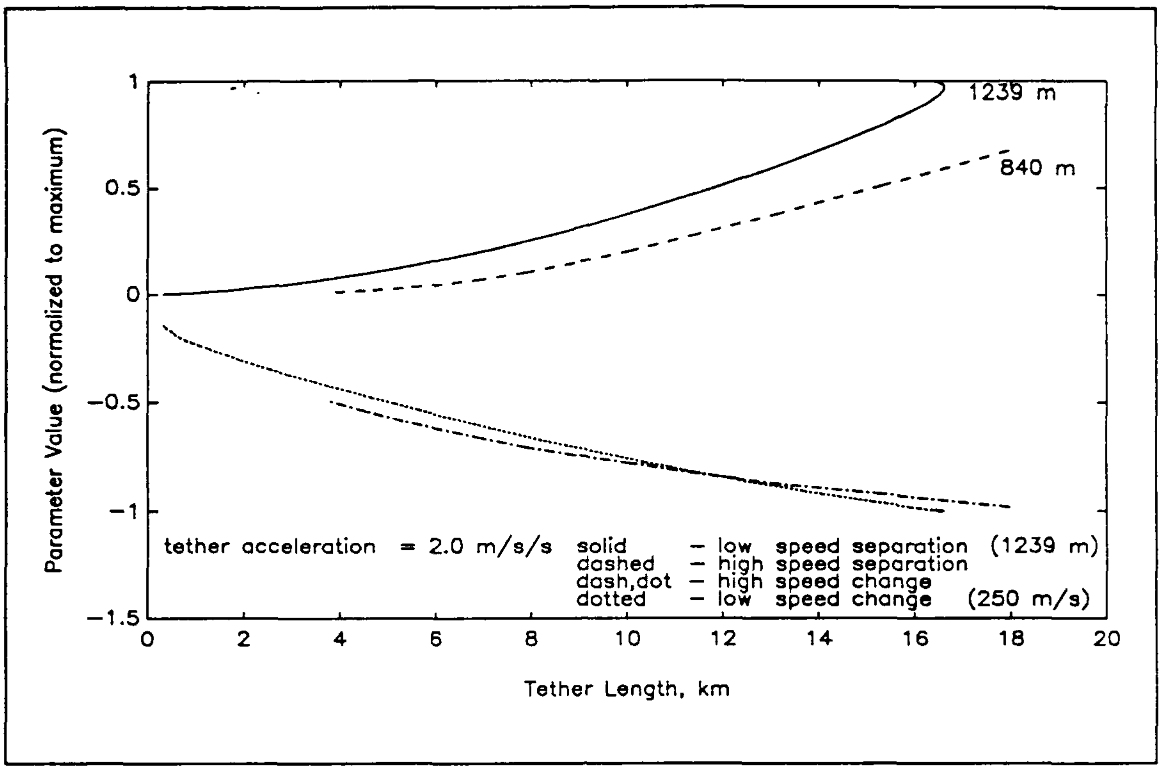

Figure 4.6 - High and Low Ejection Speed Comparison

V Conclusions and Recommendations

Various parameters affect the minimum payload separation during reel-in tethering. The mission duration, number of free and full arc cycles, and ejection velocity were varied to determine their affect on minimum separation. All assessments were performed for optimum trajectories, which are generally preferred.

1 Conclusions

Increasing mission duration causes increased minimum separation while increasing tether length. Additionally, increased propulsion capability is attained with increased mission durations. Thus, if a safe separation is desired, any optimum trajectory with an equal or greater minimum separation is satisfactory.

Trajectories that optimally terminate with a negative radial rate (prior to reaching the minimum separation point) have increased minimum separation over the peri-orbiter radius. However, since the difference is small, the peri-orbiter radius is an effective model for minimum separation.

A decrease in ejection speed decreases propulsion capability. However, although it decreases separation for a specific mission duration, it increases separation for a specific tether length. Thus, a specific tether length has a range of minimum separations for varied ejection speeds.

Overall, essentially any minimum separation for an optimum trajectory can be achieved by varying tether length or ejection speed. Variation of both may or may not provide sufficient optimum propulsive capability depending on additional factors such as the tether acceleration, the initial orbit, and the mass of the payload and orbiter.

2 Project Recommendations

Numerous conceptual operational problems exist with the reel-in tether, some of which are unique. In addition to nominal concerns about torque on the orbiter and tether tension capability, the reel-in tether requires a substantial winch capability and satisfactory tether management. During the mission, the tether length that is retrieved must be managed; while after payload release, the deployed tether length must be managed. However, although only separation has been addressed in this study, these problems may conceivably be solved in the next century. Continued study of the reel-in tether is recommended to determine complete propulsive capability and prompt the investigation, and hopefully the solution, of the operational problems.

3 Recommendations for Further Study

Since the double cycle is highly desirable for decreasing tether lengths for specific mission durations, a revised or new optimization method should be applied to determine the optimum trajectories for multiple cycles. However, the single cycle case still requires continual variation of the ejection speed. Additionally, tether acceleration variations are important for determining the impact of a tether structural limit. While considerations of tether mass dynamics may be complex, simple models would allow more complete determination of minimum separation and propulsive capability.

An important area for separation is non-optimum trajectories. Variation from the optimum trajectory would clearly change the minimum separation, but would extensively increase the scope of study, as well. Of lesser concern is the resultant orbit shapes. Nonetheless, examination of the final orbits of the payload and orbiter may warrant investigation.

4 Summary

The reel-in tether provides a unique method of propelling a payload and orbiter. The major dynamic disadvantage, low minimum separation, can clearly be investigated for a range of pertinent operations. Overall, safe separation is not an obstacle for the feasibility of a reel-in tether.

BIBLIOGRAPHY

1. Abramowitz, Milton and Stegun, Irene A. *Handbook of Mathematical Functions*. New York: Dover Publications, Inc., 1972.

2. Battin, Richard H. *An Introduction to the Mathematics and Methods of Astrodynamics*. New York: AIAA Press, 1987.

3. Bekey, Ivan. "Tethers Open New Space Options," *Astronautics and Aeronautics*, 21: 33-40 (April 1983).

4. Bekey, Ivan and Penzo, Paul A. "Tether Propulsion," *Aerospace America*, 24: 40-43 (July 1986).

5. Beyer, William H. *CRC Standard Mathematical Tables*(26th Edition). Boca Raton, FL: CRC Press, Inc., 1973.

6. Colombo Giuseppe, et al, "Use of Tethers for Payload Orbital Transfer," Appendix A. Smithsonian Astrophysical Observatory, NAS8-33691, March 1982.

7. De Matteis, Guido. "Dynamics of a Tethered Satellite in Elliptical, Nonequatorial Orbits," *29th Aerospace Sciences Meeting*. (7-10 January 1991). AIAA-91-0532

8. Forward, Robert L. "The Cable Catapult," *AIAA/SAE/ASME/ASEE 26th Joint Propulsion Conference*. (16-18 July 1990).

9. Gradshteyn, I. S. and Ryzhik, I. M. *Tables of Integrals, Series and Products*. New York: Academic Press, 1965.

10. Grossi, Mario D. "Historical Background Leading to the Tethered Satellite System (TSS)," *AIAA 24th Aerospace Sciences Meeting*. (6-9 January 1986). AIAA-86-0048

11. Jani, Yashvant and Lea, Robert N. "Fuzzy Logic Captures Human Skills," *Aerospace America*, 29: 25-27 (October 1991).

12. Kopke, Kenneth D. and others. "Newtonian Derivation of the Equations of Motion for a Tethered Satellite System," *Proceedings of the 1990 AIAA/AAS Astrodynamics Conference*. 875-887. Washington: AIAA Press, 1990.

13. Santangelo, Andrew D. and Johnson, Glen E. "Stability of a Tethered Satellite System," *29th Aerospace Sciences Meeting*. (7-10 January 1991). AIAA-91-0474

14. Wiesel, William E. "Optimal Payload Lofting with Tethers," *Journal of Guidance, Control, and Dynamics*, 11: 352-356 (July-August 1988).

15. Wiesel, William E., Professor of Astronautics. Personal interview. Air Force Institute of Technology, Wright-Patterson AFB OH, 1 January-30 November 1991.

16. Wiesel, William E. *Spaceflight Dynamics*. New York: McGraw-Hill, Inc., 1989.

Vita

Captain Jay H. Rothhaupt was born in Pennsylvania and graduated from Gettysburg Senior High School in 1979. He completed the U.S. Air Force Basic Military Training School at Lackland AFB in 1979 and the Automatic Tracking Radar Technician and the Technical Training Instructor courses at Keesler AFB in 1980. He then served as a Master Instructor of Radar and Computer Electronics with the 3395th Technical Training Group, Air Training Command, at Keesler AFB, MS from July, 1980 to January, 1983. During this period, Capt Rothhaupt graduated from the Community College of the Air Force with an Associate of Applied Science Degree in Ground Radar Technology. Captain Rothhaupt subsequently attended the Pennsylvania State University under the U.S. Air Force Airman Engineering and Commissioning Program from March, 1983 to August, 1985, graduating with a Bachelor of Science in Aerospace Engineering. He was commissioned a second lieutenant at the U.S. Air Force Officer Training School in November, 1985, and then served as a NAVSTAR Global Positioning System Satellite Engineering Instructor with the 2d Satellite Control Squadron at Falcon AFB, CO. During the transition from civilian to military crew operations for the GPS Master Control Station, he developed the MCS Space Segment instructional system and instructed spacecraft dynamics, contingency operations, and the spacecraft operations for the first operational (Block II) NAVSTAR spacecraft launch. Captain Rothhaupt also served as the 2d Space Wing GPS Configuration Control Officer at Falcon AFB and attended Squadron Officer School at Maxwell AFB, AL in 1990 prior to entering the Air Force Institute of Technology School of Engineering in May, 1990.

REPORT DOCUMENTATION PAGE

[illegible]

1. AGENCY USE ONLY (Leave blank)

2. REPORT DATE
December 1991

3. REPORT TYPE AND DATES COVERED
Master's Thesis

4. TITLE AND SUBTITLE
Propulsive Capability of a Reel-in
Tether with Safe Separation between
Payload and Orbiter

5. FUNDING NUMBERS

6. AUTHOR(S)

Jay H. Rothhaupt, Captain, USAF

7. PERFORMING ORGANIZATION NAME(S) AND ADDRESS(ES)

Air Force Institute of Technology, WPAFB OH 45433-6583

8. PERFORMING ORGANIZATION REPORT NUMBER

AFIT/GA/ENY/91D-10

9. SPONSORING/MONITORING AGENCY NAME(S) AND ADDRESS(ES)

10. SPONSORING/MONITORING AGENCY REPORT NUMBER

11. SUPPLEMENTARY NOTES

12a. DISTRIBUTION/AVAILABILITY STATEMENT

Approved for public release; distribution unlimited

12b. DISTRIBUTION CODE

13. ABSTRACT (Maximum 200 words)

This study investigates the use of a massless reel-in tether for propulsion of a payload following deployment from an orbiter. The distance between the payload and orbiter at closest passage is addressed. A literature review revealed several tether concepts, extensive tether research, and numerous mathematical models. However, previous work in the area of reel-in tethers is limited to propulsion feasibility. The reel-in tether is operated following optimum ejection of the payload from the orbiter using a free arc and subsequent full arc. The free arc of zero tether tension provides initial separation. Switching to a full arc of continuously-maximum tension at the optimum time accelerates and propels the payload until the mission is complete. Tether and winch capabilities are assumed to be satisfactory during the arcs. Families of trajectories are examined for a range of mission times and minimum final payload energy. Families for two ejection speeds provide comparison of propulsion capability, tether length, and minimum separation radius. Safe separation is achievable through variation of the mission duration and/or the ejection speed.

14. SUBJECT TERMS
Tethers, Tethering, Tethered Satellites

15. NUMBER OF PAGES
71

16. PRICE CODE

17. SECURITY CLASSIFICATION OF REPORT	18. SECURITY CLASSIFICATION OF THIS PAGE	19. SECURITY CLASSIFICATION OF ABSTRACT	20. LIMITATION OF ABSTRACT
Unclassified	Unclassified	Unclassified	UL